



Review

Heteroatom-Doped Porous Carbon-Based Nanostructures for Electrochemical CO₂ Reduction

Qingqing Lu¹, Kamel Eid^{2,*}  and Wenpeng Li^{1,3} 

¹ Engineering & Technology Center of Electrochemistry, School of Chemistry and Chemical Engineering, Qilu University of Technology (Shandong Academy of Sciences), Jinan 250353, China; qqllu@qlu.edu.cn (Q.L.); liwenpeng@qlu.edu.cn (W.L.)

² Gas Processing Center (GPC), College of Engineering, Qatar University, Doha 2713, Qatar

³ Shandong Key Laboratory of Biochemical Analysis, College of Chemistry and Molecular Engineering, Qingdao University of Science and Technology, Qingdao 266042, China

* Correspondence: kamel.eid@qu.edu.qa

Abstract: The continual rise of the CO₂ concentration in the Earth's atmosphere is the foremost reason for environmental concerns such as global warming, ocean acidification, rising sea levels, and the extinction of various species. The electrochemical CO₂ reduction (CO₂RR) is a promising green and efficient approach for converting CO₂ to high-value-added products such as alcohols, acids, and chemicals. Developing efficient and low-cost electrocatalysts is the main barrier to scaling up CO₂RR for large-scale applications. Heteroatom-doped porous carbon-based (HA-PCs) catalysts are deemed as green, efficient, low-cost, and durable electrocatalysts for the CO₂RR due to their great physiochemical and catalytic merits (i.e., great surface area, electrical conductivity, rich electrical density, active sites, inferior H₂ evolution activity, tailorable structures, and chemical–physical–thermal stability). They are also easily synthesized in a high yield from inexpensive and earth-abundant resources that meet sustainability and large-scale requirements. This review emphasizes the rational synthesis of HA-PCs for the CO₂RR rooting from the engineering methods of HA-PCs to the effect of mono, binary, and ternary dopants (i.e., N, S, F, or B) on the CO₂RR activity and durability. The effect of CO₂ on the environment and human health, in addition to the recent advances in CO₂RR fundamental pathways and mechanisms, are also discussed. Finally, the evolving challenges and future perspectives on the development of heteroatom-doped porous carbon-based nanocatalysts for the CO₂RR are underlined.

Keywords: doped carbon; heteroatom; porous carbon CO₂ reduction; CO₂ conversion; metal-free electrocatalysts; electrochemical CO₂ reduction



Citation: Lu, Q.; Eid, K.; Li, W. Heteroatom-Doped Porous Carbon-Based Nanostructures for Electrochemical CO₂ Reduction. *Nanomaterials* **2022**, *12*, 2379. <https://doi.org/10.3390/nano12142379>

Academic Editor: Francesc Viñes Solana

Received: 23 May 2022

Accepted: 6 July 2022

Published: 12 July 2022

Publisher's Note: MDPI stays neutral with regard to jurisdictional claims in published maps and institutional affiliations.



Copyright: © 2022 by the authors. Licensee MDPI, Basel, Switzerland. This article is an open access article distributed under the terms and conditions of the Creative Commons Attribution (CC BY) license (<https://creativecommons.org/licenses/by/4.0/>).

1. Introduction

The incessant utilization of fossil fuels as energy sources as well as industrialization result in greenhouse gas emissions (GHGs) and other hazardous gases that are the main reason for the environmental catastrophes that threaten life on planet Earth, such as climate change and global warming [1–4]. Among GHGs, CO₂ alone contributes ~20%; the CO₂ emission level increased from ~390 ppm in 2012 to 420 ppm in 2021, but nearly 1% of this amount is being removed annually [1]. Finding green energy resources (i.e., fuel cells [5–10], solar cells [11,12], water electrolysis [13–16], and batteries [17,18]), CO₂ capture [19,20], and CO₂ conversion [1] are the main approaches to reducing CO₂ levels in the Earth's atmosphere. CO₂ can be easily converted to high-value-added chemicals and fuels (i.e., alcohols, acids, CO, and methane) using reforming (i.e., steam and dry), photocatalytic, and biological CO₂RR [21–25]. The electrochemical CO₂RR is promising as an efficient and green approach, owing to its ambient operating conditions (i.e., room temperature, atmospheric pressure, controllable production of various products under adjustable potential) [21–23]. This is driven by various metals/oxides (i.e., Cu, Ru, Ir, Rh, TiO₂, SnO₂, and CeO₂), metal

chalcogenides (i.e., ZnTe, SnS₂, and CdS), carbon nitrides, metal–organic frameworks, and perovskites [26–32].

Unlike these catalysts, carbon materials are deemed as greener, efficient, low-cost catalysts feasible for practical CO₂RR [33–37]. Heteroatom (i.e., N, P, O, B, halogens)-doped porous carbon nanostructures (HA-PCs) possess many advantages compared with other carbon-based catalysts. This is owing to their intrinsic physicochemical merits (i.e., metal-free nature, chemical durability, thermal stability), unique catalytic merits (i.e., outstanding surface area to volume ratio, high electrical conductivity, rich electrical density, accessible active sites, low H₂ evolution activity, and tailorable structures), and distinctive properties of porous structures (i.e., maximized atom utilization, quick electron mobility, ease of gas adsorption, and diffusion) [33,38–45]. HA-PCs could be easily produced in a high yield (i.e., kilogram scale) from green, earth-abundant, and cheap resources (i.e., carbohydrate, cellulose, and lignin) that can meet the sustainability and large-scale application requirements [44,46–48]. Thereby, the engineering of porous carbon materials for CO₂RR has attracted significant attention in the last decade, resulting in nearly 750 articles; meanwhile, 53 are exclusively dedicated to HA-PCs for CO₂RR (Figure 1a). Accordingly, it is imperative to provide a timely update on this theme of CO₂RR executed on HA-PCs. Notably, various reviews have been published for the CO₂RR using carbon-based catalysts; however, they were not all related to HA-PCs (Table 1) [34,49–53].

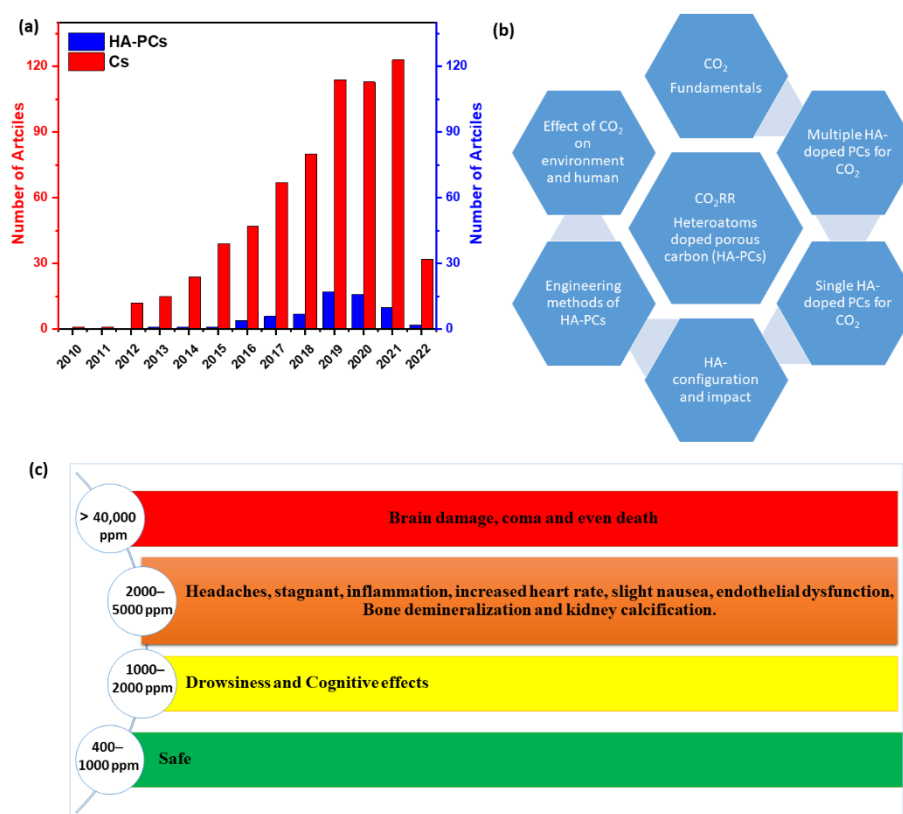


Figure 1. (a) Number of published articles related to carbon-based catalysts (Cs) and heteroatom-doped porous carbon catalysts (HA-PCs) for CO₂RR obtained from the Web of Science using keywords “carbon-catalysts for electrochemical CO₂ reduction” and “porous carbon-doped”. (b) The focus of this review and (c) the effect of CO₂ on human health.

Table 1. Summary of the main reviews related to porous doped carbon-based nanostructures for CO₂RR compared with the present review.

Title	Focus	Ref.
Heteroatom-Doped Porous Carbon-based Nanostructures for Electrochemical CO ₂ reduction	Engineering of heteroatom (i.e., N, S, P, and B)-doped porous carbon materials for the electrochemical CO ₂ reduction reaction (CO ₂ RR). The effect of mono, binary, and ternary dopants on CO ₂ RR, and their fundamentals and mechanisms, are discussed, in addition to the effect of CO ₂ on the environment and human health.	This work
Heterogeneous Single-Atom Catalysts for Electrochemical CO ₂ Reduction Reaction	Synthesis of metal single-atom catalysts (SACs) supported carbon, graphene, and metal–organic framework for CO ₂ RR to CO and its fundamental mechanism.	[49]
Advanced Heteroatom-Doped Porous Carbon Membranes Assisted by Poly(ionic liquid) Design and Engineering	Controlling structures and properties of heteroatom-doped porous carbon membranes (HPCMMs) using porous polymer membranes as sacrificial templates built up from heteroatom-rich poly(ionic liquid) for fuel cells and water electrolysis applications.	[54]
Metal-Free Carbon Materials for CO ₂ Electrochemical Reduction	Fabrication of carbon-based catalysts (i.e., carbon fibers, carbon nanotubes, graphene, diamond, nanoporous carbon, and graphene dots) doped with heteroatoms (e.g., N, S, and B) for the CO ₂ RR as well as the identification of active sites and pathways.	[50]
Carbon-Supported Single Metal Site Catalysts for Electrochemical CO ₂ Reduction to CO and Beyond	Fabrication of metal single-atoms embedded in carbon-based SACs (denoted as MN _x C _y , where M = Ni, Fe, and Co) for electrocatalytic CO ₂ RR to CO, C1, and C2 products. This is in addition to the effect of precursors and synthetic conditions on the structure of SACs.	[34]
Rational confinement engineering of MOF-derived carbon-based electrocatalysts toward CO ₂ reduction and O ₂ reduction reactions	The fabrication methods of MOF-derived carbon-based electrocatalysts supported (atoms, atomic clusters, and nanoparticles) for oxygen reduction reaction and CO ₂ RR.	[51]
Carbon-rich nonprecious metal single atom electrocatalysts for CO ₂ reduction and hydrogen evolution	The fabrication process of carbon (diamond, MOF, graphene, nanotubes, etc.)-supported single-atom (Ni, Co, Fe, Zn, and Sn) catalysts for CO ₂ RR and supported single-atom (Ni, Co, Fe, Mo, and W) catalysts for hydrogen evolution reaction.	[52]
Atomically Structural Regulations of Carbon-Based Single-Atom Catalysts for Electrochemical CO ₂ Reduction	The fabrication and characterization of carbon-supported metal single-atom catalysts for CO ₂ RR in addition to the recent progress in controlling coordination structures of heteroatom coordination, coordination numbers, diatomic metal centers, and the microenvironments for CO ₂ RR catalytic performance.	[53]

In pursuit of this aim, this review highlights the engineering approaches of HAPCs for the electrochemical CO₂RR in addition to the effect of mono, binary, and ternary heteroatoms (i.e., N, S, F, or B) on the CO₂RR activity, durability, and selectivity from both experimental and theoretical views (Figure 1b). This is in addition to underlining the CO₂RR pathway and mechanisms along with the current challenges and perspectives on developing heteroatom-doped porous carbon nanocatalysts for the CO₂RR.

2. Effect of CO₂ on the Environment and Human Health

CO₂ emissions come from industrial activities (32%), building operations (28%), transportation (23%), building materials and construction (11%), and other sources (6%) and are one of the main reasons for global warming and climate change, which affect humans and the environment significantly [1,55]. CO₂ absorbs a lower heat than other greenhouse gases, but it remains in the atmosphere longer and acts as a blanket in the air, trapping heat in the

atmosphere and warming up the Earth's temperature and increasing the temperature of the ocean ($0.07\text{ }^{\circ}\text{C}/\text{decade}$) [1,55]. Increases in Earth's temperature lead to several environmental changes (i.e., shrinking H_2O supplies, geographic weather patterns, food supplies, acid rains, and sea level). Moreover, CO_2 reacts with the H_2O of the ocean to produce carbonic acid, which decreases the ocean's pH, reducing the ability of marine life to extract calcium from the water to build their shells [55]. Humans are exposed daily to CO_2 indoors and outdoors, including inside homes, workplaces, and streets; CO_2 is a product of human metabolism and is respired into the ambient air. The average CO_2 indoors ranges from 600 to 1000 ppm but can reach 2000 ppm with increased room occupancies and poor ventilation rates [56]. Thus, the effect of CO_2 on human health should usually be emphasized and studied, as was extensively discussed in another review [56]. Excessive exposure to CO_2 can lead to increased heart rate, blood pressure, difficulty breathing, brain damage, coma, and even death, depending on CO_2 concentration and exposure time [57]; Figure 1c depicts the effect of CO_2 on human health as a factor of concentration and exposure time. The concentration of CO_2 indoors or outdoors should not exceed 1000 ppm for more than 2.5 h to avoid any hazardous effects. Meanwhile, the dangerous effects of exposure to CO_2 comprise inflammation at 2000–4000 ppm for 2 h, cognitive effects at 1000–2700 ppm for 1–6 h, bone demineralization/kidney calcification at 2000–3000 ppm for 60–90 days, behavioral changes/physiological stress at 700–3000 ppm for 13–15 days, oxidative stress/endothelial dysfunction at 3000–5000 ppm for 13 days to 6 months, and brain damage or death at 40,000 ppm [56,57]. Interestingly, it has been revealed that CO_2 can be stored inside the human body, as indicated by the significant increase in serum bicarbonate in the general US population [58,59]. Few studies have reported the direct effect of CO_2 on human health; therefore, more experimental and theoretical studies are needed [56].

3. Fundamental Parameters for CO_2RR Performance

The fundamental parameters for estimating the CO_2RR performance are the Faradaic efficiency (FE), overpotential, current density, durability, and energy efficiency [1,53].

3.1. Faradaic Efficiency (FE)

The FE is calculated from the following equation:

$$\text{FE} = nmF/Q,$$

where n , m , F , and Q are the number of electrons, total mole amounts of the product, Faraday constant ($96,485\text{ C/mol}$), and amounts of cumulative charge during CO_2 reduction. The FE determines the CO_2RR selectivity for various gas/liquid products (i.e., CH_4 , CO , HCOOH , and CH_3OH), so a higher FE for specific products is highly required to reduce the cost of isolation products. A catalyst with an inferior HER ability is desired to yield a great FE and high selectivity, which could be enhanced via the integration of heteroatom dopants into the carbon skeleton structure and modifying the hydrophobicity of electrodes. Organic and hybrid electrolytes can also improve the FE due to their great CO_2 adsorption ability and higher solubility of CO_2 during CO_2RR ; however, the effect of electrolytes on CO_2RR activity and selectivity is not yet resolved and remains ambiguous [34,49–53].

3.2. Overpotential

The CO_2RR half-reaction under applied potential, which is a nonspontaneous process driven by more negative potentials than standard potentials in actual electrocatalytic conditions, results in various products. The difference between the standard thermodynamic potential of a specific half-reaction and the applied potential in the half-cell reaction is the overpotential. This is often used to activate inert CO_2 molecules to form a bent $^*\text{CO}_2^{\bullet-}$ anion radical and allow electron transport during the CO_2RR process. The lower overpotential is desired to mimic the practical process and reduce the CO_2RR production cost, which could be achieved by modulating carbon-based catalysts' morphology and composition. The CO_2RR can occur through a single and multiple proton-coupled electron transfer

process, so carbon-based materials with tunable structures and properties are thermodynamically feasible for single electron and multiple electron transfer processes [34,49–53].

3.3. Partial Current Density

The partial current density (j_p) represents the current density needed for the production of specific products, and it is calculated using the following equation:

$$j_p = j \times FE$$

where j is the total current density, so the effective catalyst should deliver a high j_p under a low applied potential. The j_p depends on the inherited catalytic properties of HA-PCs (i.e., electrical conductivity, interaction with the electrode, and CO₂ adsorption) in addition to the electrolyte and cell design [34,49–53]. The flow cell system allows prompt CO₂ feeding into the cathode with the assistance of a gas diffusion electrode, resulting in an outstanding j_p . Notably, to date, the obtained total current density is lower than 1 A, which is still far beyond commercial requirements [34,49–53].

3.4. Durability

The durability of FE and current density are some of the essential factors hinging on CO₂RR with maintained selectivity and activity under prolonged potentiostatic polarization. Notably, durability tests are carried out for a few hours, which is insufficient for the large-scale CO₂RR applications; however, currently, most of the catalysts are exposed to significant attenuation in the current density, FE, and selectivity, owing to blocking and deactivation of the active catalytic sites and structural degradation. In light of the commercialization scale, the stability tests should be conducted for several weeks or months (≥ 1000 h) along with carrying out various in situ and ex situ characterizations to understand the degradation mechanism and solve this critical issue. Carbon-based catalysts, with their impressive chemical–physical stability, are promising to solve the stability issues in CO₂RR, but they are not investigated enough. The modification of the electrochemical cell to allow continued CO₂ flow, refreshing the electrolyte solution, preventing gas accumulation over the cathode, and gathering liquid products, can enhance the long-term stability of porous carbon-based catalysts [34,49–53].

3.5. Energy Efficiency (E_{eff})

The E_{eff} is a crucial factor in estimating the economic efficiency of CO₂RR as it is the percentage of the energy stored in the chemical. The E_{eff} is calculated based on the equilibrium potential (E_{eq}) using the following equation:

$$E_{eff} = [E_{eq}/E_{eq} + \eta] \times EF$$

Thus, a great E_{eff} together with outstanding catalytic activity drives the CO₂RR half-reaction at a low η , negligible ohmic potential drop, and high FE. The high E_{eff} is optimized via adjusting the electrolyte, membrane, and cell structure in addition to carbon-based electrode conductivity. Notably, the relationship between the structure/composition of HA-PC catalysts and E_{eff} is not yet studied [34,49–53].

3.6. Turnover Frequency (TOF)

TOF is the amount for generating specific products over single active sites per unit time during CO₂RR process, so it is an imperative factor toward the intrinsic activity of HA-PCs. The TOF is calculated from the following equation:

$$TOF = N_p/N_c$$

where N_p and N_c are the product's mole number and the mole number of the catalyst's active site, respectively. A high TOF value indicates the presence of multiple active sites.

Porous carbon-based doped materials usually possess a high TOF for gas products, especially CO, but the effect of the shape and composition of porous carbon-based catalysts with heteroatoms has not yet been emphasized [34,49–53].

4. Engineering Methods of Heteroatom-Doped Porous Carbon

There are limited approaches for the fabrication of template-based, activation, element-doping, and direct annealing of biomass-based resources, which vary in their productivity for controlling porosity (i.e., pore-volume, pore ordering, and pore size) and surface area [34,49–53].

4.1. Template-Based Method

The template-based method is the most effective approach for the rational synthesis of HA-PCs with well-defined morphology, surface area, and ordered porosity driven by the template shape, structure, and properties. There are various hard templates (i.e., MgO, AlO, CaCO₃, ZnO, and SiO₂), soft templates (i.e., surfactants, polymers, and ionic liquids), and self-templates (i.e., biomass and metal–organic frameworks (MOFs)) or their hybrids [60–63]. The carbon precursors should be initially infiltrated into the template and annealed at an elevated temperature, followed by chemical etching of the template in acid or alkaline solutions. The source for heteroatoms can be mixed initially with the carbon source to produce heteroatom-doped porous carbon nanostructures.

4.1.1. Hard Templates

With its unique physiochemical properties, the ZnO template can generate porous carbon with 1D (i.e., nanorods and nanotubes) and 3D nanostructures via the incorporation of activators (i.e., KOH). ZnO is easily prepared commercially at a low cost via Zn's electrochemical anodic oxidation method under ambient conditions. Moreover, carbon precursors react with ZnO at a high temperature to produce CO₂ gas that acts as an activator to enhance the porosity and surface area. Notably, Zn tends to evaporate via an annealing process at 900 °C, resulting in eliminating the need for acids or alkali solution to remove the ZnO template. Porous core/shell carbon microrods with a high surface area of 660 m²/g were prepared using a ZnO microrod template and glucose as a carbon source (Figure 2a–c) [64].

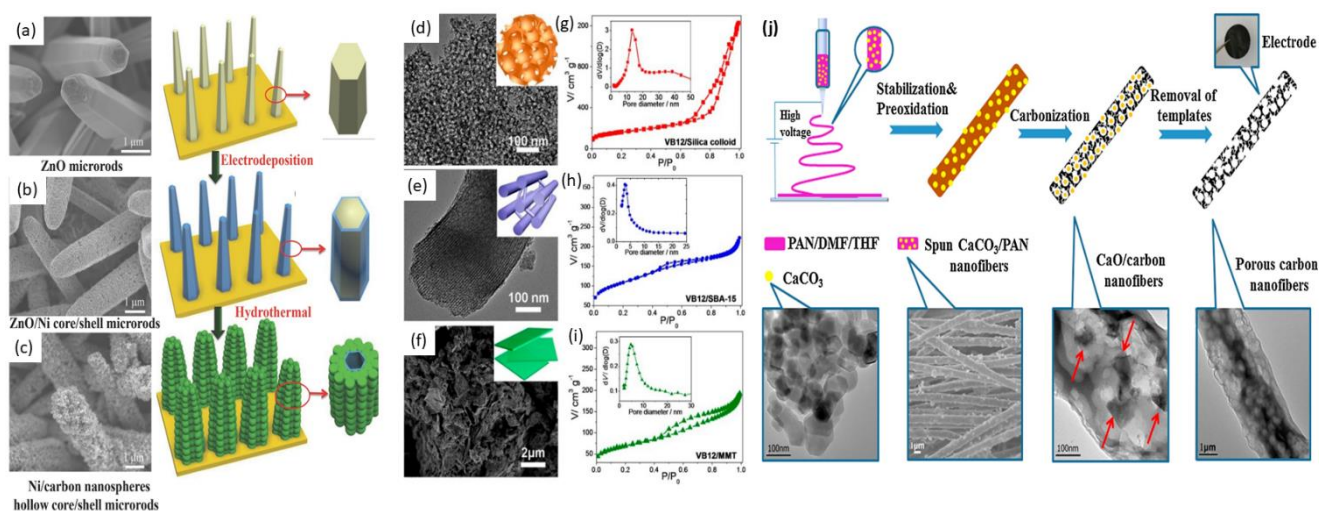


Figure 2. (a–c) SEM images and preparation process of porous core/shell carbon microrods using ZnO microrods template. Reprinted with permission from [64]. Copyright 2015 Wiley. TEM image and BET surface area of porous carbon prepared using (d,g) colloidal SiO₂, (e,h) ABA-15, and (f,i) MMT templates. Reprinted with permission from [65]. Copyright 2013 American Chemical Society. (j) The fabrication process with its related SEM and TEM images of hierarchical porous carbon nanofibers formed using CaCO₃ template. Reprinted with permission from [66]. Copyright 2016 Elsevier.

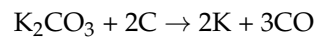
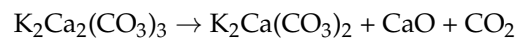
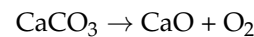
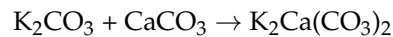
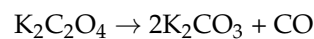
ZnO microrods on Ni-foil were initially designed by chemical bath deposition, then coated with Ni metals by electro-deposition, and then coated with glucose via autoclave at 180 °C for 3.5 h, followed by annealing at 500 °C under Ar (Figure 2a–c). At 500 °C, glucose is carbonized into carbon nanospheres coated with porous microrods formed from ZnO's evaporation. Three-dimensional flower-like hierarchical porous carbon nanostructures with a surface area of 761.5 m²/g, pore volume of 0.49 cm³/g, and microporosity of 49% were prepared via a ZnO template in the presence of HO as an activator [67]. With its unique crystal structure, MgO acts as a template for producing porous 2D sheets, 3D clusters, and 2D/3D nanostructures [68]. Mesoporous 3D carbon nanosheets with a BET surface area (883 m²/g) and pore size (6–8 nm) were synthesized using a MgO template and coal tar pitch as the carbon source, followed by washing with 10% HCl to remove MgO [69]. Porous carbon nanocages (CNC670) with a surface area of 2053 m²/g and pore size of 3–7 nm were obtained using MgO as the template and benzene as a carbon source via annealing at 670 °C and then removal of MgO by HCl [70]. Notably, annealing at a high temperature of 700, 800, and 900 °C led to decreasing the surface area to 1854, 1633, and 312 m²/g, respectively. Other Mg-based materials could also be used as a template for the production of HA-PCs, because they can produce in situ MgO templates. Hierarchical porous carbon nanosheets with a surface area of 2300 m²/g were formed using starch as a reductant and carbon source while Mg(NO₃)₂ was an oxidant and in situ provided a MgO template [71]. Similarly, layered porous carbon nanosheets with a surface area of 1312 m²/g were formed via the combustion of pectin with Mg(NO₃)₂ [72]. Three-dimensional carbon nanocage networks with a surface area of 1470–1927 m² g⁻¹ and pore size of 15–24 nm were formed via annealing of the pitch with Mg₅(CO₃)₄ and KOH treatment [73]. Porous carbon sheets with a surface area of 3145 m²/g and abundant micropores were formed via annealing of coal tar pitch with Mg(OH)₂ and in situ KOH activation [74]. Carbon nanocages with a surface area of 3368 m²/g and pore volume of 1.7 cm³/g were formed using Mg metal and CO₂ as precursors [75].

There are various types of SiO₂-based templates (FSM-16, MCM-48, KIT-6, and SBA-15) that can drive porous carbon nanostructure formation with a well-defined shape and porosity. Co/N-doped mesoporous 3D carbon nanostructures with a surface area of 568 m²/g and pore size of ~12 nm were formed using colloidal SiO₂ as a template and vitamin B12 as a template (VB12/Silica colloid) (Figure 2d–i) [65]. Under the same condition, using SBA-15 produced porous nanorods (VB12/SBA-15) with a surface area of 387 m²/g and pore diameter of 3.5 nm, while 2D carbon nanosheets with a surface area of 239 m²/g and pore size of 4.5 nm were obtained using montmorillonite silica as a template (VB12/MMT) (Figure 2d–i) [65]. N-doped porous carbon nanosheets with a surface area of 1676 m²/g and large pore volume of 2.13 cm³/g were formed via SiO₂ spheres as a template and polyaniline as the C/N source, followed by KOH activation at 850 °C [76]. Without KOH activation, the same group synthesized 2D mesoporous carbon layered nanosheets with a surface area of 582.7 m²/g using mesoporous SiO₂ nanoplates as a template and coal tar pitch as the carbon source, which implies the significant role of activation on the enhancement of the pore volume and surface area [77]. Si-based precursors such as tetraethylorthosilicate (TEOS) could be used to allow in situ formation of SiO₂ via the hydrolysis process and could act as in situ templates for the production of porous carbon [78]. A mesoporous porous carbon microsphere with a surface area of 659–872 m²/g and mesopore diameter of 3.2–14 nm was fabricated using TEOS within resorcinol–formaldehyde polymer microspheres and NH₄OH as a catalyst, followed by annealing [79].

4.1.2. Ca-Based Templates

CaCO₃ can act as a template and activator due to its ability to decompose at 500 °C to release CO₂ (activator); the CaO template forms hierarchical porous carbon with multiple pores (i.e., micro-, meso-, and macropores) after the removal of CaO. Hierarchical porous carbon nanofibers (HPCNFs-3-1) with a surface area of 679 m²/g and pore volume of 0.41 cm³/g were prepared via the electrospinning of polyacrylonitrile (PAN) (as the C/N

source)/N, N'-dimethylformamide (DMF)/tetrahydrofuran (THF) with nano-CaCO₃ (as a template) followed by carbonization at 800 °C for 2 h and then template removal by 1.5 M HCl (Figure 2j) [66]. Under annealing, nano-CaCO₃ decomposes to release CO₂ that produces microspores and mesopores. Then, CaO removal by HCl creates macropores and changes the ratios of PAN/DMF/THF, having an insignificant effect on the surface area and pore volume of the resultant porous carbon fibers. N-doped hierarchical porous carbon with a surface area of 1091 m²/g, pore volume of 0.52 cm³/g, and N content of 10.59% was synthesized via annealing of gelatin and graphene oxide with CaCO₃ at 900 °C and then activation by KOH. The activation substantially affected the surface area and pore volume because, without activation, they decreased to 433 m²/g and 4.5 cm³/g, respectively [80]. Cornstalk rind (whole plant) was annealed with CaCO₃ and K₂C₂O₄ (activator) at 800 °C to hierarchical porous carbon with a surface area of 2054 m²/g and pore volume of 1.382 cm³/g [81]. The surface area (1419–2054 m²/g) and pore volume (0.3704–1.382 cm³/g) were regulated via adjustment of the activation ratio by K₂C₂O₄ but without activation of the surface area (482 m²/g) [81]. The following equations propose the reaction between CaCO₃ and K₂C₂O₄:



Similarly, crumpled carbon network-like nanosheets with a surface area of 1822 m²/g and pore volume of 4.11 cm³/g were formed using annealing anthracene oil with CaCO₃ as a template coupled with KOH activation [82]. Other Ca-based sources such as Ca(NO₃)₂ and Ca(OH)₂ could be used as templates and activation for directing the formation of porous carbon nanostructures, but they have rarely been reported.

4.1.3. New Templates

Various new templates such as dry ice (CO₂), MXene, and melamine can act as a template for producing HA-PCs. Dry CO₂ produces porous carbon with a lower surface area (100 m²/g), so other templates or activation are needed to enhance the surface area and porosity. Mixing phenolic resin, triblock copolymer F127, and Ti₃C₂T_x MXene followed by annealing and chlorination formed a 2D/2D porous heterostructure with a surface area of 1021 m²/g and a pore volume of 58% (Figure 3a) [83]. F127 and phenolic resin molecules are assembled into spherical micelles, which penetrate the interlayers of Ti₃C₂T_x to form Ti₃C₂T_x-micelle@resol. Then after annealing, Ti₃C₂T_x-micelle@resol is converted into porous carbon (Ti₃C₂T_x-OMC), and the removal of Ti in Ti₃C₂T_x-OMC produces MXene-derived porous carbon (MDC-OMC) [83]. The chlorination of MDC-OMC at high temperature severely impacted the increment of the surface area and pore volume of MDC-OMC [83].

Hierarchical porous carbon tunable porosity (i.e., micro-, meso-, and macroporous), a surface area of ~2500 m²/g, and a pore volume of ~11 cm³/g were formed via annealing of colloidal silica with sucrose at 1000 °C followed by removal of SiO₂ before being activated by CO₂ at 900 °C [85]. Honeycomb-like porous carbon nanosheets with a surface area of 2038 m²/g and pore volume of 1.07 cm³/g were synthesized from the coal tar pitch using melamine as a soft template coupled with KOH activation [86].

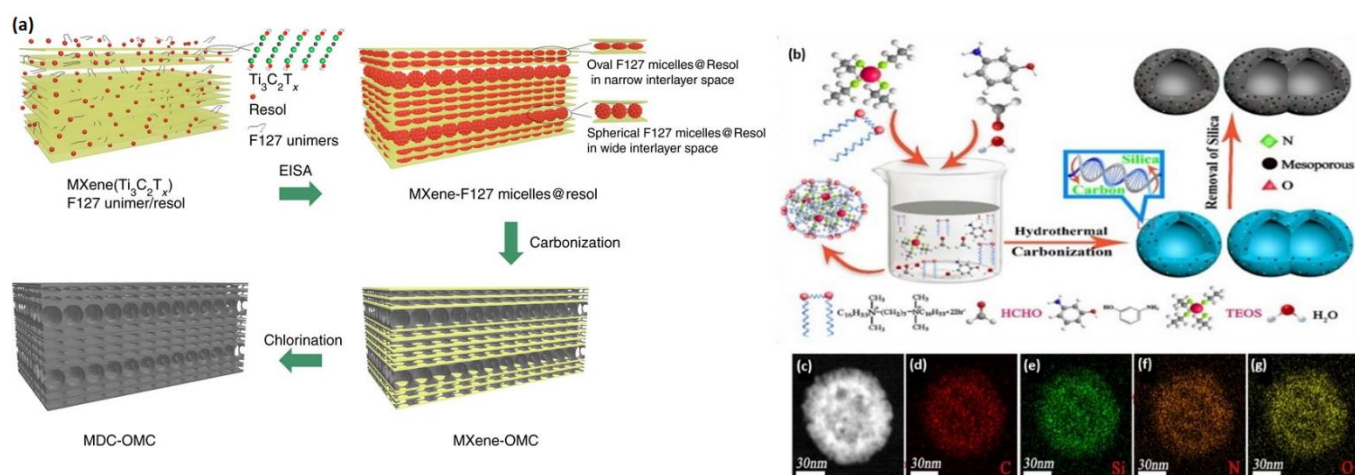


Figure 3. (a) The preparation process of MXene-derived porous carbons (MDC-OMCs). Reprinted with permission from [83]. Copyright 2017 Nature. (b) The synthesis mechanism, (c) HAADF-STEM, and (d–g) element mapping of N/O-doped porous carbon nanospheres using Gemini surfactant template. Reprinted with permission from [84]. Copyright 2020 Elsevier.

4.1.4. Organic Soft Templates

Ionic copolymers (i.e., cetrimonium bromide, cetrimonium chloride, and Gemini-type) and non-ionic copolymers (i.e., Pluronic F127, polyvinylpyrrolidone, Brij) are the common organic templates for the production of HA-PCs. N-doped (4.16–6.74 %) hierarchical mesoporous carbon spheres with a tunable size (30–140 nm), great surface area (1215–1517 cm^2/g), large pore volume (1.12–3.22 cm^3/g), and open interconnected mesoporous structure (5–20 nm) were synthesized using Gemini surfactant pentane-1,5-bis(dimethylcetyl ammonium bromide) in ethanol via the sol-gel method based on the interfacial reaction mechanism (Figure 3b) [84]. The obtained nanoparticles had a spherical size of 95 nm with a good distribution of C (69.23%), N (3.29%), O (19.77%), and Si (7.86%) (Figure 3c–g). Changing the amount of Gemini surfactant substantially increased surface area and porosity, but the TEOS was also used to generate a SiO_2 template that was etched by hydrofluoric acid.

N,O,S-enriched hierarchical porous carbon foam with a surface area of 2685 m^2/g was made using 1,3,5-trimethyl benzene (TMB) and Pluronic 407 (F127) as a soft template in the presence of graphene oxide, dopamine (DA), and cysteine through the freeze-drying and chemical etching method (Figure 4a) [87]. F127 and TMB are assembled on graphene oxide into micelles coated with polydopamine obtained from the self-polymerization of dopamine into the surface of spherical micelles driven by the shearing force. Regardless of the difficulty of this approach, an additional activation step by KOH is needed.

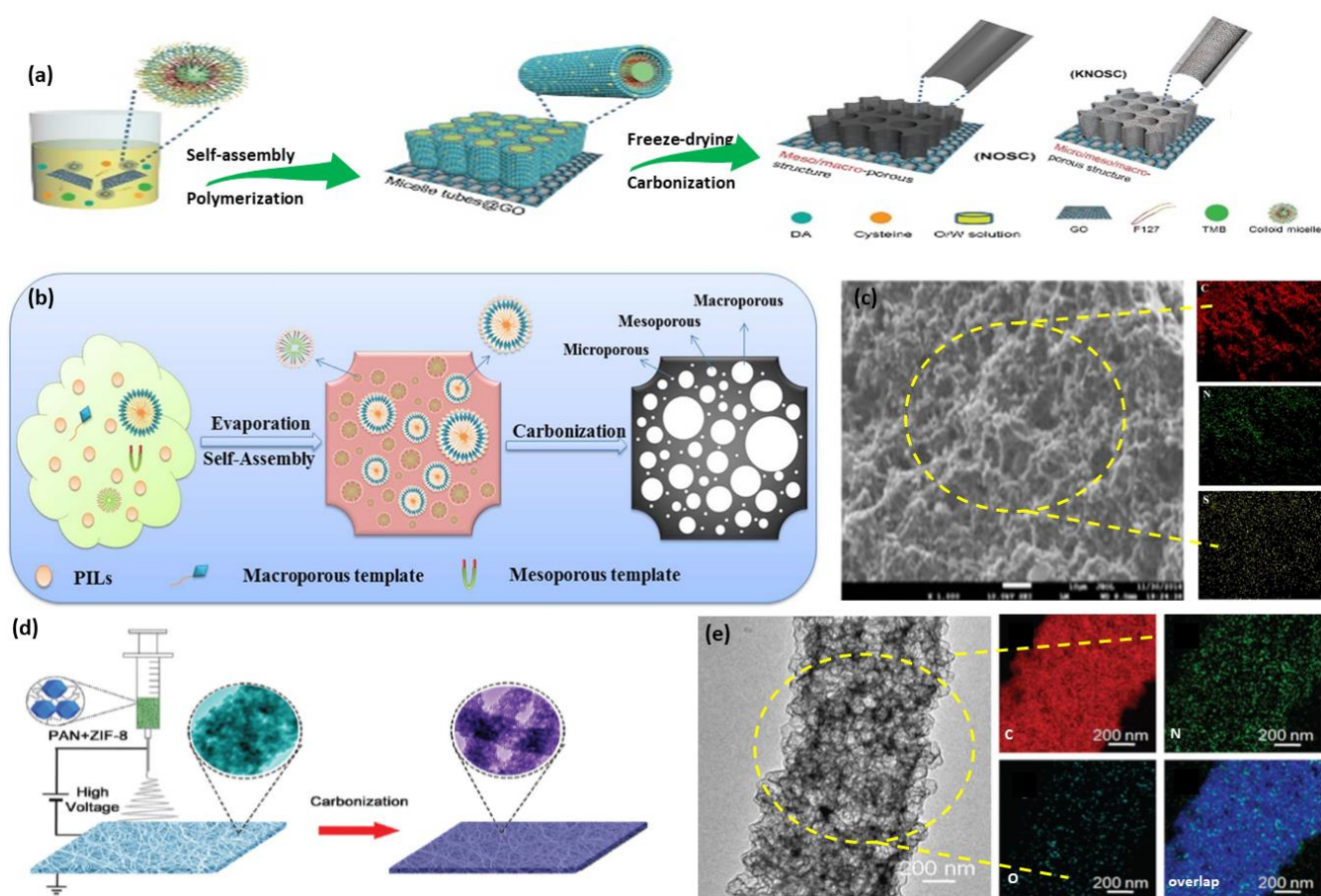


Figure 4. (a) The formation process of N,O,S-enriched hierarchical porous carbon foam. Copyright 2019 Wiley [87]. (b) The formation process and (c) SEM image with elemental mapping of N/S-co-doped hierarchical porous carbon nanosheets. Reprinted with permission from [88]. Copyright 2017 American Chemical Society. (d) The preparation method and (e) TEM image with its elemental mapping of N-doped hollow carbon nanofibers formed using ZIF-8 template. Reprinted with permission from [89]. Copyright 2017 Royal Society of Chemistry.

4.1.5. Ionic Liquids

With their thermal durability, small vapor pressure, and inbuilt heteroatoms, ionic liquids are commonly used as the precursors and templates to prepare heteroatom-doped porous carbon nanostructures. N/B-doped porous carbon nanosheets with a surface area of $2000 \text{ m}^2/\text{g}$ and pore volume of 2.75 mL/g were prepared using Bmp-dca and Emim-tcb ionic liquids as carbon precursors and templates with eutectics as a porogen at $1400 \text{ }^\circ\text{C}$ [90]. Notably, porogen could be easily recovered for reusability, and the obtained surface area ($2000 \text{ m}^2/\text{g}$) of the resultant carbon is superior to zeolite, activated carbons, and graphene. Moreover, the salt templating method is feasible for the large-scale and sustainability requirements.

N/S-co-doped hierarchical porous carbon nanosheets with a surface area of $575 \text{ m}^2/\text{g}$ and pore volume of $0.55 \text{ m}^3/\text{g}$ were formed using the self-assembly and carbonization of [Phne][HSO₄], a protic ionic liquid, as the N/C/S source in addition to acting as a template with and soft template of OP-10 and F-127 (Figure 4b,c) [88]. Changing the ratios of [Phne][HSO₄]/F-127/OP-10 leads to changing the surface areas and pore volume; meanwhile, OP-10/F-127 is easily decomposed during annealing at $700 \text{ }^\circ\text{C}$ to produce porous carbon foam with a good distribution of C, N (3.41%), and S (6.65%) (Figure 4c) [88]. This process is applicable for other ionic liquids with and without soft templates for the formation of HA-PC nanostructures.

Three-dimensional porous carbon nanosheets with a surface area of $1593 \text{ m}^2/\text{g}$ and pore volume of $0.85 \text{ cm}^3/\text{g}$ were formed via coal tar using 1-butyl-3-methylimidazolium tetrafluoroborate (BMIMBF₄) ionic liquid as a template at $800 \text{ }^\circ\text{C}$ and in situ KOH activation [91]. Essentially, coal tar pitch transforms into polynuclear aromatic polymers at initial heating and BMIMBF₄ decomposes at $500 \text{ }^\circ\text{C}$, creating 3D interconnected pores coherently distributed within obtained carbon. The activation pivots significantly in increments of the surface area and pore volume. The utilization of ionic liquid for synthesizing carbon nanostructures is not emphasized enough, and their mechanisms remain ambiguous and not profoundly investigated. In addition, the high cost, the difficulty of preparation, and the air-sensitive nature of ionic liquids are crucial barriers to their commercialization.

Deep eutectic solvents (DESs) are novel ionic liquids consisting of Lewis or Brønsted acids and alkaline eutectic mixture systems. Unlike traditional ionic liquids, they possess outstanding physiochemical merits such as ionic strength, polarity, supramolecular structure, dielectric constant, inferior vapor pressure, biodegradability, low cost, and durability without environmental sound, which enables their utilization as a carbon source, templates, and solvents in the synthesis of porous doped carbon nanostructures [92].

Notably, utilization of DESs in the fabrication of porous carbon nanostructures is rarely reported and not studied enough compared with other templates. N/O-enriched hierarchically nanoporous carbon with a surface area of $1414 \text{ m}^2/\text{g}$ and pore volume of $\sim 0.55 \text{ cm}^3/\text{g}$ was synthesized through the direct annealing of DESs of urea and ZnCl₂ with phenol-formaldehyde resin 85. This allowed a high content of N (8.09 at.%) and O (14.77 at.%) tunable surface area/pore volume via adjusting the composition of the DESs and their ratio to resin. N/O-doped hollow carbon nanorods with a surface area of $1086 \text{ m}^2/\text{g}$ were prepared by direct carbonization of DESs (urea, 2,5-dihydroxy-1,4-benzoquinone, and ZnCl₂) as sources of N/O/C and as a template [93]. ZnCl₂ can act as a dehydration agent and pore modulator as it can generate ZnO as a self-template for the generation of mesopores and macropores.

4.1.6. MOF Template

MOFs act as sources of carbon and self-templates for various kinds of porous carbon nanostructures, owing to their unique properties such as tunable chemical compositions, porosity, and surface area [51]. During the thermal decomposition process, the metal species inside MOFs can be directly used as the template. N-doped hollow carbon nanofibers with a surface area of $443.5 \text{ m}^2/\text{g}$ and pore volume of $1.6 \text{ cm}^3/\text{g}$ were synthesized via annealing of zeolite imidazole framework (ZIF-8) nanoparticles into electrospun polyacrylonitrile (PAN) at $800 \text{ }^\circ\text{C}$ (Figure 4d) [89]. The electrospinning of PAN with ZIF-8 forms nanofibers that are carbonized into porous carbon fiber (Figure 4e) at high temperatures, while Zn in ZIF-8 can form ZnO that acts as a template, and increasing the annealing temperature leads to decreasing the surface area and pore volume. The N and O contents were about 9.39% and 4.94%, respectively, as confirmed by the elemental mapping analysis (Figure 4e). The derived BET and Langmuir surface areas were 1192 and $1678 \text{ m}^2/\text{g}$, respectively, with a large pore volume of $1.06 \text{ cm}^3 \text{ g}^{-1}$, which is high enough to facilitate ion transportation. Electrospinning can be used for spinning any other polymer with different MOFs to form 1D nanostructures (i.e., rods, fibers, wires) driven by various experimental parameters (i.e., applied potential and polymer concentrations). Porous carbon nanorods with a surface area of $1192 \text{ m}^2/\text{g}$ and pore volume of $1.06 \text{ cm}^3/\text{g}$ were synthesized by thermal K-MOF at 200 , 450 , and $800 \text{ }^\circ\text{C}$. K-MOF generates K₂O and carbonates at high temperatures, which act as in situ templates and activators. The same concept is feasible for Zn-MOF, Ni-MOF, and Co-MOF because they can also create metal-oxides that act as templates and activators. We briefly emphasized MOF-derived porous carbon nanostructures because it was deeply discussed before in another review [51].

4.1.7. Biomass-Derived Carbons

Porous carbon nanostructures with various 1D, 2D, and 3D morphologies can be easily prepared via the direct annealing of biomass wastes from plant wastes, animals, insects, and microbes, which are low-cost, biodegradable, earth-abundant, unique porous structures and inherent heteroatoms, producing carbon nanostructures with outstanding electrical conductivity, massive active sites, and unique physicochemical properties. Moreover, biomass with its hierarchical porous structures (i.e., rods, sheets, nanotubes) acts as a carbon source and template for generating various porous morphologies under ambient conditions. N,S co-doped porous carbon nanosheets with a surface area of $1533 \text{ m}^2/\text{g}$ and pore volume of $0.92 \text{ cm}^3/\text{g}$ were synthesized via the one-step thermal decomposition at $400 \text{ }^\circ\text{C}$ and KOH activation at $850 \text{ }^\circ\text{C}$ of the biomass of willow catkin fibers [94].

B/N co-doped carbon nanosheets with a surface area of $416 \text{ m}^2/\text{g}$ and a pore volume of $0.76 \text{ cm}^3/\text{g}$ were created via annealing of gelatin biomass with boric acid at $900 \text{ }^\circ\text{C}$ [95]. The same approach is vulnerable to other biomasses. N-doped hierarchical porous carbon with a surface area of $315 \text{ m}^2/\text{g}$ and pore volume of $0.65 \text{ cm}^3/\text{g}$ was prepared from Bohai shrimp shell with KOH and CaCO_3 at $700 \text{ }^\circ\text{C}$ [96]. CaCO_3 acts as a self-template, while activation with KOH creates abundant micropores and mesopores [96]. The removal of CaCO_3 significantly affected surface area and porosity. Soft templates and activators can be used with biomass to create porous carbon nanostructures. Moreover, selecting biomass with abundant heteroatoms is essential to allow in situ generation of heteroatom-enriched porous carbon. Notably, various plant wastes have not yet been investigated for the formation of HA-PCs. Meanwhile, previously reported biomass-derived porous carbon nanostructures have rarely been studied for CO_2RR compared with other applications such as supercapacitors.

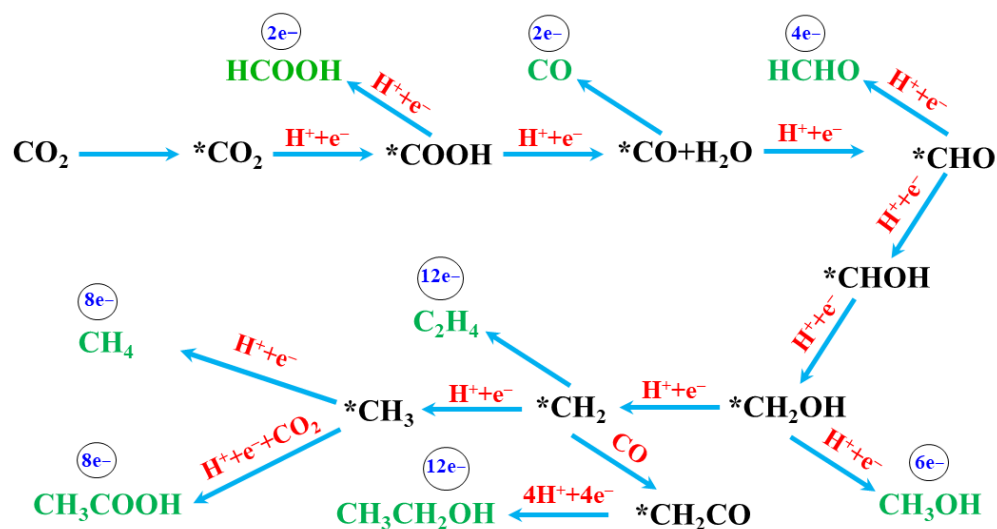
4.2. CO_2RR Pathways

CO_2 is a valuable molecule, and CO_2RR can generate wide ranges of high value-added hydrocarbons and gases (i.e., CO and CH_4 , CH_3OH , $\text{C}_2\text{H}_5\text{OH}$, and HCOOH) driven by the applied potentials (Table 2) and electron transfer number (Scheme 1). This is based on the catalyst compositions and experimental parameters (i.e., applied potential, cell type, and electrolyte) via different CO_2RR pathways. The CO_2RR pathways on carbon-based catalysts generally include multiple interactive steps of CO_2 adsorption and charge transfer, including electron and proton transfer in addition to product dissociation, which comprises migration of the products from the catalyst surface. The CO_2 molecule is very stable thermodynamically with a great dissociation energy of $\sim 750 \text{ kJ/mol}$ for $\text{C}=\text{O}$ (which needs significantly greater energy), which is greater than that of other carbon-based chemical bonds, such as $\text{C}-\text{H}$ ($\sim 430 \text{ kJ/mol}$) and $\text{C}-\text{C}$ ($\sim 336 \text{ kJ/mol}$). Notably, the applied potential in CO_2RR is often much more negative than the equilibrium potential, resulting in high overpotential. This is because the CO_2 adsorption comprises the rearrangement of a linear CO_2 molecule to a bent radical anion via one-electron transfer to a CO_2 molecule (i.e., $\text{CO}_2 + \text{e}^- \rightarrow \text{CO}_2^{\bullet-}$, $E^0 = -1.9 \text{ V}$). During this process, the $\text{C}=\text{O}$ bond is strongly unstable, and the electrons are shared between the CO_2 and the catalyst. The obtained $\text{CO}_2^{\bullet-}$ radical is highly reactive and easily reacts with H_2O in the electrolyte to produce HCO_2^{\bullet} that is perturbed and tends to transform to HCO^* , which is consequently released from the active catalyst sites. These multiple electron transfers and protonation processes occur on carbon-based catalysts to produce various products. The E^0 for most CO_2RR half-reactions is close to 0 V vs. RHE (Table 2), so the undesired side products because of the HER ($2\text{H}^+ + 2\text{e}^- \rightarrow \text{H}_2$, $E^0, 0.42 \text{ V}$) result in the reduced electrocatalytic CO_2RR activity of carbon-based catalysts. The CO_2RR pathways can lead to the formation of various products driven by electron transfer and protonation under different applied potentials (Scheme 1). Experimental studies using in situ analysis and computational calculations (i.e., density functional theory (DFT)) were used to confirm the CO_2RR mechanisms and pathways. Mainly after the CO_2 activation, protonation can occur for O to form $^*\text{COOH}$ or C to produce $^*\text{OCHO}$. HA-PC catalysts $^*\text{COOH}$ pathways are preferred over $^*\text{OCHO}$, so they

usually produce CO in addition to HCOOH via the two-electron reduction process with rare CH₃CH₂OH. This is due to the absence of stable adsorbed states for the *HCOOH and *CO on the heteroatom-doped carbon surface for facilitating protonation of the *COOH intermediate. Despite the great progress in CO₂RR, its mechanism and the boundary between each reaction pathway remain ambiguous owing to the absence of effective methods to detect the intermediates.

Table 2. Electrode potentials (E⁰) vs. standard hydrogen electrode (SHE) of the selected CO₂RR in aqueous solutions at pH = 7 and 25 °C based on data from Refs. [97,98] (pH = 7 in aqueous solution vs. standard hydrogen electrode (SHE), 25 °C, 1-atmosphere gas pressure, and 1 M concentration of solute).

Half Reactions of CO ₂ R	E ⁰ /V vs. SHE
$\text{CO}_2 + \text{e}^- \rightarrow \text{CO}_2^-$	-1.90
$\text{CO}_2 + 2 \text{H}^+ + 2 \text{e}^- \rightarrow \text{HCOOH}$	-0.61
$\text{CO}_2 + 2 \text{H}^+ + 2 \text{e}^- \rightarrow \text{CO} + \text{H}_2\text{O}$	-0.53
$\text{CO}_2 + 4 \text{H}^+ + 4 \text{e}^- \rightarrow \text{HCHO} + \text{H}_2\text{O}$	-0.48
$\text{CO}_2 + 6 \text{H}^+ + 6 \text{e}^- \rightarrow \text{CH}_3\text{OH} + \text{H}_2\text{O}$	-0.38
$\text{CO}_2 + 8 \text{H}^+ + 8 \text{e}^- \rightarrow \text{CH}_4 + 2\text{H}_2\text{O}$	-0.24
$2 \text{CO}_2 (\text{g}) + 10 \text{H}_2\text{O} (\text{l}) + 14\text{e}^- \rightarrow \text{C}_2\text{H}_6 (\text{g}) + 14 \text{OH}^-$	-0.270
$3 \text{CO}_2 (\text{g}) + 13 \text{H}_2\text{O} (\text{l}) + 18\text{e}^- \rightarrow \text{C}_3\text{H}_7\text{OH} (\text{l}) + 18 \text{OH}^-$	-0.320
$2 \text{CO}_2 (\text{g}) + 9 \text{H}_2\text{O} (\text{l}) + 12\text{e}^- \rightarrow \text{C}_2\text{H}_5\text{OH} (\text{l}) + 12 \text{OH}^-$	-0.33
$2 \text{CO}_2 (\text{g}) + 8 \text{H}_2\text{O} (\text{l}) + 12\text{e}^- \rightarrow \text{C}_2\text{H}_4 (\text{g}) + 12 \text{OH}^-$	-0.34



Scheme 1. The proposed CO₂RR pathways on HA-PCs.

4.3. Heteroatom-Doping Configuration and Effects

4.3.1. Advantages of Heteroatoms

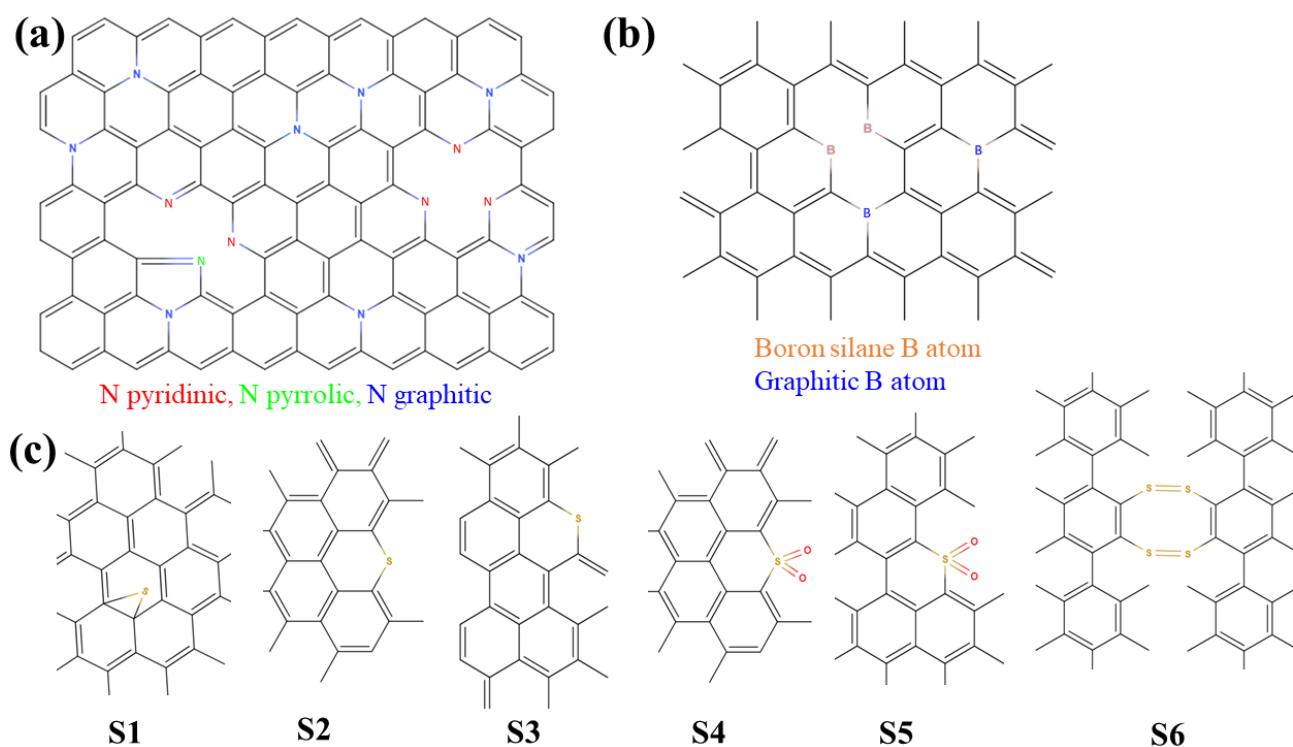
There are various metal-based catalysts for CO₂RR; however, their high cost, earth scarcity, and ability for the HER are critical barriers to large-scale applications and sustainability requirements. To this end, noble metals (i.e., Pt, Pd, Ru, and Au) possess great activity for the HER, while Au, Ag, and Sn, for example, produce mainly C1 (e.g., CO and HCOOH) rather than C2 products via a two-electron transfer pathway. Cu/Cu–O forms low-carbon hydrocarbons and oxygenates (i.e., CO with relatively high overpotentials). HA-PCs are promising electrocatalysts for the CO₂RR with remarkable catalytic activity, long durability, and high selectivity. Distinct from metal-based catalysts, porous carbon

materials possess numerous advantages such as tailorable structures/properties, rich specific surface chemistry, excellent surface area to volume ratio, thermal–chemical–physical durability, and low toxicity.

Moreover, C can be easily synthesized in high yield from inexpensive and natural abundant resources that meet the sustainability requirements. During CO₂RR, HA-PCs tune the adsorption of CO₂, induce electrolyte–electrode interaction, provide massive catalytic active sites, maximize atomic utilization, and tolerate the adsorption of intermediates and products. The HER activity of porous carbon catalysts is inferior, so the undesired effect of HER during CO₂RR is neglected. The CO₂RR is carried out in aqueous electrolyte solutions, so the electrode's wettability or hydrophilicity is crucial to controlling the transportation of hydrated CO₂ to the active sites. Heteroatom dopants enhance the hydrophilicity of the C-electrode, which can promote the accessibility of reactants to the active sites; make active sites more accessible, thus maximizing atomic utilization during the CO₂RR. Integration of heteroatoms (i.e., P, N, O, B, and S) into carbon skeleton structures is essential to detect the limitation of electrical conductivity of carbon-based catalysts to empower their CO₂RR activity. This is due to electron-donating or electron-withdrawing properties of heteroatoms that modulate the electronic characteristics.

4.3.2. Nitrogen (N) Configuration and Effects

The N atom is an ideal heteroatom for modulating the properties of carbon due to its size (155 pm) being close to that of the carbon atom (170 pm). In addition, N has a larger electronegativity (3.04) than carbon (2.55), so N-doped C (N–C) can attract electrons, create multiple active sites, and augment the electronic/ionic conductivity of carbon. The N atom in the C skeleton structure is mainly pyridinic (398.5 eV), pyrrolic/pyridonic (400.1 eV), quaternary, or graphitic (401.1 eV), and pyridine-N-oxide (403.2 eV), that can be easily identified by X-ray photoelectron spectroscopy (XPS) [99]. These N species (Scheme 2a) are highly active sites for CO₂RR and other catalytic applications. N-doping introduces Lewis basicity on C's surface that endows the CO₂ adsorption significantly.



Scheme 2. The proposed configuration of HA-PCs, including (a) N-doped, (b) B-doped, (c) and S-doped, based on data from Refs. [99–101].

4.3.3. Boron (B) Configuration and Effects

The smaller size of the B atom (85 pm) and its lower electronegativity (2.04) than C lead to the retention of the planar structure of C. The XPS showed two in-plane binding structures in B-doped C, including graphitic B at 200.5 eV, B atoms substituting for C atoms in the hexagonal ring, and “boron silane” B at 198.5 eV, referring to the place of B in the co-conjugated system (Scheme 2b) [99]. B-doping persuades charge polarization in the C framework, stabilizes the negatively polarized O atoms in CO₂, and consequently enhances the chemisorption of CO₂ on C during the CO₂RR process due to the relatively large electropositivity between B and C atoms.

4.3.4. Sulfur (S) Configuration and Effects

Stone–Wales defects ease the formation of S-doping into carbon. The relatively larger size of the S atom (180 pm) and higher electronegativity (2.58) than C lead to improving C’s electrical conductivity and provide a higher spin density, edge strain, and charge delocalization. There are four types of S dopant in C, including S1, S2/S3, S4/S5, and S6 for adsorption of S on the C surface, the substitution of C by S at the edges, formation of the S/S oxide at the edges, and S-containing ring connecting sheets, respectively, as confirmed by DFT on a graphene model (Scheme 2c) [100]. The formation energies for these species are different, but S1 is the most durable structure.

4.3.5. Phosphorus (P) Configuration and Effects

The P atom has a lower electronegativity (2.19) and greater electron-donating ability than the C atom and generates positive charges on the P dopant and negative charges on positively charged C, introducing new functional groups (P⁺–C[−]) which change the structure of C, resulting in accelerated charge transfer and the reduced binding energy of intermediates. Also, the P atom, with its size (195 pm) being larger than C, leads to various defects in C skeleton structures, which act as active sites during CO₂RR. Usually, P-doping occurs through the substitution of C by P. The XPS can detect P dopant at 130.2 eV, P–C at (132.5 eV), and P–O at (134.0 eV).

4.3.6. Oxygen (O) Configuration and Effects

The oxygen (O) atom has a lower atom size (152 pm) than C but a greater electronegativity (3.44 pm) that enhances positive charges on C to form (C⁺–O[−]) after doping, which can attract electrons, create multiple active sites, and enhance the electronic/ionic conductivity of C. Also, introducing O into the carbon framework creates abundant structural defects and modulates the inherent electronic structure, allowing tuning adsorption/desorption of reactants and intermediates during CO₂RR. Moreover, O-doping creates various functional groups (i.e., C–O, C=O, and C–OH) which can promptly activate oxidants allowing in situ generations of reactive oxygen species, activating H₂O₂ to in situ form oxygenated species that facilitate the CO₂RR kinetics. The O-doping occurs via partial substitution of C with O to form C–O at (532 eV) and C=O at 533 eV species, as confirmed by the XPS, which are highly active sites for CO₂RR. The FTIR can also easily detect the O-doping.

4.4. Single Heteroatom-Doped Porous Carbon Materials

Because the stable sp² or sp³ hybridized carbon atoms cannot activate CO₂ molecules, pristine carbon materials possess poor electrocatalytic activity for CO₂RR. Therefore, incorporating heteroatoms with different electronegativity into carbon provides a great opportunity to modulate the electronic properties and thus improve their catalytic performance [50,102]. Porous carbons have unique advantages such as high specific surface area and tunable pore structure, which is beneficial for mass transfer and abundant active sites, thereby increasing the catalytic activity [103–105]. According to the reported literature, the frequently used single dopant can be classified into nitrogen, boron, sulfur, and fluorine [33]. Table 3 shows a detailed comparison of the electrocatalytic performance of binary HA-PCs toward CO₂RR.

4.4.1. Nitrogen-Doped Porous Carbon Materials

Nitrogen is one of the most widely studied dopants for carbon materials, based on the fact that the nitrogen atom has a similar atomic size to the carbon atom and higher electronegativity of 3.04 compared to the carbon atom's 2.55. N-doping can induce more electrons into the carbon matrix and thus improve the electrical conductivity. Moreover, more active sites can be created after the N-doping [106–108]. As displayed in Figure 5A, the N dopants can exist in four types: pyridinic N, pyrrolic N, graphitic N, and oxidized N [109]. Liu et al. developed a series of N-doped carbon catalysts with tunable types and contents of nitrogen dopants to uncover the correlation between N species and catalytic performance toward CO₂RR [110]. Electrochemical tests coupled with X-ray photoelectron spectroscopy identified that the CO₂RR activity is proportional to the content of pyridinic N, whereas no noticeable relevance was observed on other N species. Moreover, the free energy calculated by density functional theory (DFT) calculations in Figure 5B revealed that the COOH could interact with pyridinic N in optimal bonding strength, benefiting the reduction of CO₂ to form *COOH, and further to *CO. Apart from the pyridinic N content, porous carbon materials' pore structure also affects the electrochemical performance [106,109,111–115]. For instance, N-doped nanoporous carbon sheets were synthesized by Yao et al. via a hydrothermal reaction and calcining Typha in NH₃ [116]. It was found that the calcination temperature has a significant effect on the pore structure and N atom type. The optimal sample possesses the highest surface areas and pore volume, exposing abundant accessible pyridinic N, thereby delivering a much higher selectivity of 90% for CO at a lower overpotential of −0.31 V. However, there remains controversy about the critical active N sites for CO₂RR [117]. For example, Liu and co-workers verified that the stable graphitic nitrogen atoms restricted in the micropores for coal-based metal-free electrocatalysts could effectively convert CO₂ into CO [118]. Huang's group demonstrated that pyridinic and graphitic N are the active sites for CO₂RR by calcinating oxygen-rich Zn-MOF-74 precursors at different temperatures [119].

Up to now, the reported products for N-doped porous carbon materials toward CO₂RR mainly focus on C1 compounds such as CO, CH₄, and HCOOH [121,122]. It remains a challenge to stabilize the active C1 intermediates for their coupling to generate multi-carbon products. It is worth mentioning that Song et al. developed a nitrogen-doped ordered cylindrical mesoporous carbon (denoted as c-NC) as a high-efficient catalyst for the electroreduction of CO₂ to ethanol with nearly 100% selectivity [120]. To reveal the unique structural effect of c-NC, an inverse mesoporous N-doped carbon with a similar pore structure and N content, namely i-NC, was synthesized as a control. It can be seen from Figure 5C that both c-NC and i-NC electrodes exhibit an obvious reduction peak in CO₂ saturated 0.1 M KHCO₃ solution, whereas no reduction peak was observed in Ar, indicating that the CO₂RR occurs on c-NC and i-NC. Figure 5D shows the Faradaic efficiency (FE) of CO₂RR on c-NC and i-NC catalysts at a potential between −0.40 and −1.00 V. The main product for c-NC and i-NC catalysts is ethanol from CO₂RR and H₂ from the hydrogen evolution reaction (HER), accompanied by a small amount of byproduct CO. This demonstrates that the mesoporous structure of both c-NC and i-NC contributes to the generation of ethanol. For c-NC, ethanol is the dominant product at the potential between −0.40 and −0.90 V, and the ethanol FE attained the maximum of 77% at −0.56 V. Meanwhile, the competitive reaction over c-NC for CO₂ electroreduction to CO can be neglected. By contrast, the CO₂ electroreduction to ethanol over i-NC is only dominated at the potential of −0.40 and −0.50 V, and the maximum ethanol FE reaches 44% at −0.50 V. After that, the HER becomes dominant, accompanied by a substantial amount of CO. Electrochemical impedance spectroscopy (EIS) was measured at −0.56 V vs. RHE to determine the charge transfer resistance (R_{ct}) on c-NC and i-NC catalysts (Figure 5E). The smaller R_{ct} value for c-NC (3.8 Ω) than that for i-NC (8.5 Ω) implies the easier transportation of electrons to the cylindrical surface of c-NC. DFT calculations were performed to check the possible CO₂RR reaction pathways. Both pyridinic and pyrrolic N sites can promote the adsorption/activation of CO₂ molecules and generate CO*

intermediates (Figure 5F). The calculated reaction energy for CO* formation on pyridinic and pyrrolic N sites is -1.68 and 0.12 eV, respectively, implying the preferential formation of CO* on pyridinic N sites. The CO* intermediates can be stabilized by the cylindrical surface of c-NC with high electron density, thereby restricting the CO generation. The dimerization of CO* intermediates can proceed to form OC–CO* intermediates with reaction energies of -1.31 and -0.34 eV on pyridinic and pyrrolic N sites, respectively, signifying the favorable C–C bond formation on pyridinic N sites.

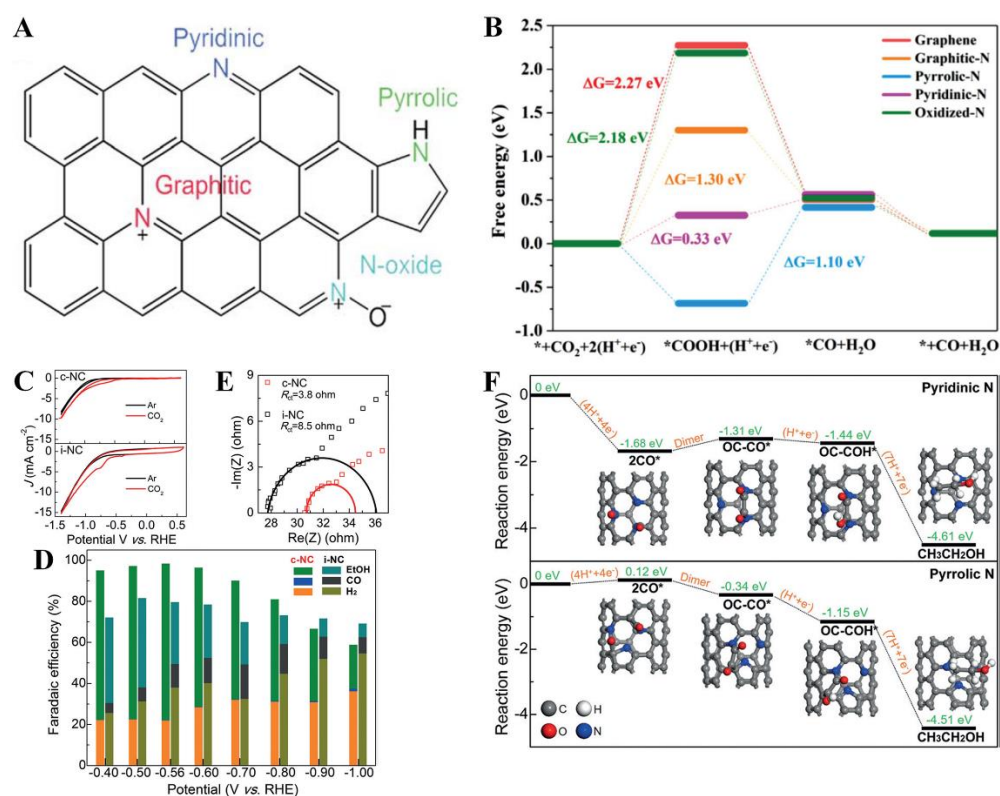


Figure 5. (A) The functional groups for N-doped carbon material. Reproduced from [109]. Copyright 2017, Elsevier. (B) Free energy diagram of CO₂RR on graphene nanoribbon networks with various nitrogen dopants. Reproduced from [110]. Copyright 2018, John Wiley & Sons (C) CVs of c-NC and i-NC catalysts at a scan rate of 5 mV/s in Ar and CO₂ saturated 0.1 M KHCO₃ solution. (D) FEs of CO₂RR on c-NC and i-NC catalysts at various applied potentials. (E) Electrochemical impedance spectroscopy (EIS) of c-NC and i-NC catalysts measured in CO₂ saturated solution at -0.56 V vs. RHE. (F) The calculated reaction energy diagrams of CO₂ electroreduction to ethanol on pyridinic and pyrrolic N sites. Adapted from [120]. Copyright 2017, John Wiley & Sons.

Moreover, the electron-rich cylindrical surface can accelerate the subsequent single and multiple proton-electron transfers to form the OC–COH* intermediate and ethanol. In short, the cylindrical surface with a high electron density and highly active N sites for c-NC synergistically benefits the highly efficient and highly selective production of ethanol. In addition, Yuan and co-workers reported the use of nitrogen-doped porous biochar from plant moss to catalyze CO₂RR into CH₄, CH₃OH, and CH₃CH₂OH at a high current density and low overpotential [123]. Except for the above-mentioned C₂ product, Li et al. first revealed that C₃ hydrocarbons could be formed during CO₂RR when nitrogen sites are situated close to each other in the micropore space [124]. Though great progress has been made for N-doped porous carbon materials, N sites' high spin density also benefits the competitive HER, resulting in moderate FE and low partial current density.

4.4.2. Other Metal-Free Heteroatom (S, F, or B)-Doped Porous Carbon Materials

Similar to N atoms, the doping of F and S atoms with electro-withdrawing or B atoms with electron-donating behaviors can also tailor the electronic structure of adjacent carbon atoms, thus improving the electrocatalytic performance toward CO₂RR [125].

Nitrogen-doped carbon nanotubes (NCNTs) with an average diameter of 30 nm and N content of 5.0% were formed via the liquid chemical vapor deposition (CVD) method using acetonitrile and dicyandiamide with ferrocene at 850 °C under Ar/H₂. NCNTs promoted the CO₂RR with a maximum FE of CO of nearly 80% at −0.78 V and an overpotential of −0.26 V, which is comparable to Au and Ag nanoparticles but with a lower overpotential in 0.1 M KHCO₃ [126]. This was significantly higher than that of N-free CNTs revealing inferior CO₂RR activity (3.5% FE_{CO}). NCNTs remain stable at −0.8 V for 10 h without any obvious degradation, and the FE varies slightly around 80% [126]. For instance, a fluorine-doped cage-like porous carbon (F-CPC) electrocatalyst was synthesized by a polymer-derived method using SiO₂ spheres as templates (Figure 6A) [127]. The transmission electron microscope (TEM) image in Figure 6B clearly shows the hollow cage-like structure of F-CPC with a thin carbon shell, in which the bright dots marked by yellow circles represent the rich mesopores on the surface. Elemental mapping images reveal that the carbon and fluorine elements homogeneously distribute throughout the F-CPC (Figure 6C,D). There is a single peak at 689.8 eV in the X-ray photoelectron spectroscopy (XPS) spectra of F 1s, suggesting the presence of a semi-ionic C–F bond in the F-CPC (Figure 6E). Compared with the covalent C–F bond, the semi-ionic C–F bond is anticipated to promote the CO₂RR. The F-CPC catalyst exhibits a maximum CO FE of 88.3% at −1.0 V vs. RHE among all samples (Figure 6F), originating from the novel structure and morphology. Moreover, the superior stability of F-CPC was confirmed by chronoamperometric curves at −0.9 V vs. RHE (Figure 6G).

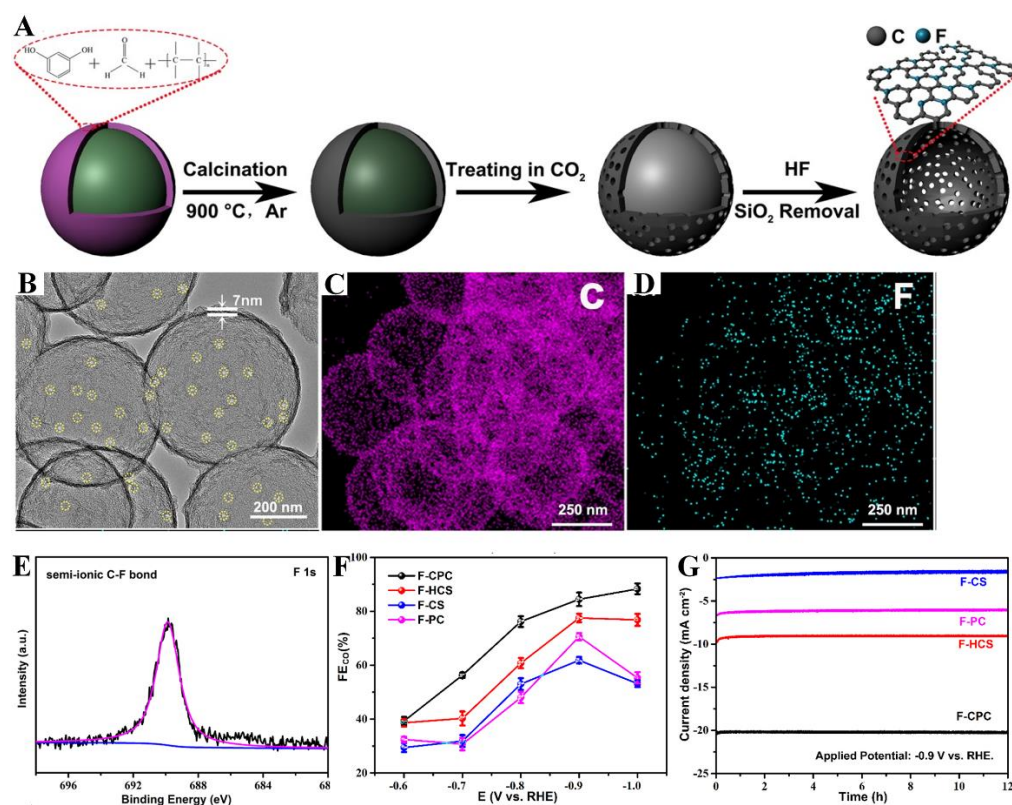


Figure 6. (A) Schematic illustration of the formation process for F-CPC. (B) TEM and (C,D) elemental mapping image of F-CPC. (E) F 1s XPS spectra of F-CPC. (F) The CO FE at various potentials for 2.5 h. (G) Chronoamperometric curves at −0.9 V vs. RHE. Adapted from [127]. Copyright 2020, American Chemical Society.

Table 3. Comparison of electrocatalytic performance of mono HA-PCs toward CO₂RR.

Electrocatalysts	Synthetic Method	Electrolyte	Main Product	Potential of FE _{max} (vs. RHE)	sFE _{max} (%) / j _{CO} (mA cm ⁻²)	Durability	Refs.
NC-900	Hydrothermal synthesis and calcination of Typha in NH ₃ at 900 °C	0.5 M KHCO ₃	CO	−0.5	82% / ~1.25 mA·cm ⁻²	FE _{CO} stability 75% after 10 h	[116]
N-GRW (GM2)	The first polymerization of melamine and L-cysteine to form C ₃ N ₄ at 600 °C, followed by carbonization at higher temperatures	0.5 M KHCO ₃	CO	−0.4	87.6% / ~7.8 mA·cm ⁻²	FE _{CO} stability 80% after 16 h	[110]
TTF-1	Thermal treatment of 2, 6- dicyanopyridine and ZnCl ₂ at 600 °C for 40 h	0.5 M KHCO ₃	CO	−0.68	82% / ~−1 mA·cm ⁻²	FE _{CO} stability 75% after 12 h	[115]
c-NC	A soft-template method via the self-assembly of resol, F127, and dicyandiamide	0.1 M KHCO ₃	CH ₃ CH ₂ OH	−0.56	77% / ~−0.35 mA·cm ⁻²	FE _{CO} stability 77% after 6 h	[120]
MNC-D	Pyrolysis of ZIF-8 at 900 °C for 3 h and mixed with HCl, followed by treatment in dimethylformamide	0.1 M KHCO ₃	CO	−0.58	~ 92% / ~−6.1 mA·cm ⁻²	FE _{CO} stability ~86% after 16 h	[108]
NPC-1000	High-temperature annealing of the mixture of oxygen-rich Zn-MOF-74 and melamine at 1000 °C	0.5 M KHCO ₃	CO	−0.55	98.4% / ~−3.01 mA·cm ⁻²	FE _{CO} stability ~98% after 21 h	[119]
NPC-900	One-step pyrolysis method via the self-assembly of anthracite coal, KOH, and dicyandiamide	0.5 M KHCO ₃	CO	−0.67	95% / ~−4.8 mA cm ⁻²	FE _{CO} stability ~80% after 10 h	[118]
BAX-M-950	Soaking commercial activated carbon BAX-1500 in a melamine suspension in ethanol followed by evaporation and drying, then heating at 950 °C in N ₂	0.1 M KHCO ₃	CO, CH ₄	−0.66, −0.76	40%, 1.2% / ~−3 mA cm ⁻²	FE _{CO} stability ~20%, 1.1% after 24 h	[111]
CNPC-1100	Etching coal powder in ammonia atmosphere	0.1 M KHCO ₃	CO	−0.6	92% / ~−4.6 mA cm ⁻²	FE _{CO} stability ~62.5% after 8 h	[112]
WNCNs-1000	An NH ₃ etching strategy by using NaCl and coal tar pitch as templates and precursor	0.1 M KHCO ₃	CO	−0.49 (over-potential)	84% / ~−1.26 mA cm ⁻²	FE _{CO} stability ~81% after 8 h	[106]
NDC-700	One-step pyrolysis of wheat flour and KOH	0.5 M NaHCO ₃	CO	−0.82	83.7% / ~−8 mA cm ⁻²	FE _{CO} stability ~79.4% after 2 h	[109]

Table 3. Cont.

Electrocatalysts	Synthetic Method	Electrolyte	Main Product	Potential of FE _{max} (vs. RHE)	sFE _{max} (%) / j _{CO} (mA cm ⁻²)	Durability	Refs.
PNC	High-temperature calcination by using melamine as the nitrogen source and pentaerythritol as the carbon source	0.1 M KHCO ₃	CO	−0.6	74%/~ −4 mA cm ⁻²	FE _{CO} stability ~70% after 10 h	[121]
N/C-Cl-1100	Halogen-assisted calcination of ZIF-8 at 1100 °C	0.1 M KHCO ₃	CO	−0.5	99.5%/~ −2.6 mA cm ⁻²	FE _{CO} stability ~99% after 20 h	[117]
HPC	Hydrothermal treatment of moss at 180 °C for 24 h, followed by pyrolyzing at 900 °C for 2 h and acidic etching	0.5 M KHCO ₃	CH ₄ , C ₂ H ₅ OH, CH ₃ OH	−1.2 (vs. Ag/AgCl)	56, 26, 10.5%/~ −15 mA cm ⁻²	FE _{CO} stability ~92.6% after 30 h	[123]
NDAPC	Pyrolysis of petroleum pitch under nitrogen atmosphere followed by ammonia etching	0.1 M KHCO ₃	CO	−0.9	83%/~ −3.76 mA cm ⁻²	FE _{CO} stability ~80% after 8 h	[113]
NG-800	The first formation of 3D graphene foam by chemical vapor deposition and post-doped with graphitic-C ₃ N ₄ , followed by etching Ni with HCl	0.1 M KHCO ₃	CO	−0.58	85%/~ −1.8 mA cm ⁻²	FE _{CO} stability ~80% after 5 h	[114]
NPC-600	Hydrothermal treatment of SBA-15 and digested sludge	0.1 M NaHCO ₃	Formate	−1.5 (vs. SCE)	68%/~ −7.5 mA cm ⁻²	FE _{CO} stability ~68% after 4 h	[122]
P-NC	The calcination of sucrose, urea, and NaCl at 800 °C for 4 h	0.5 M KHCO ₃	CO	−0.8	81.3%/~ −7.2 mA cm ⁻²	FE _{CO} stability ~81% after 6 h	[104]
NC1100	The calcination of ZIF-8 at 1100 °C in Ar	0.5 M KHCO ₃	CO	−0.5	95.4%/~ −3 mA cm ⁻²	FE _{CO} stability ~90% after 20 h	[107]
F-CPC	An aldol reaction conducted at SiO ₂ surface, followed by calcination at 900 °C, activation with CO ₂ , and removal with HF	0.5 M KHCO ₃	CO	−1.0	88.3%/~ −37.5 mA cm ⁻²	FE _{CO} stability ~85% after 12 h	[127]
FC	Pyrolyzing the mixture of commercial BP 2000 and polytetrafluoroethylene	0.1 M NaClO ₄	CO	−0.62	89.6%/~ −0.25 mA cm ⁻²	-	[128]
BG	Heating the uniform mixture of graphene oxide and boric acid at 900 °C in Ar	0.1 M KHCO ₃	HCOOH	−1.4 (vs. SCE)	66%/~ −3 mA cm ⁻²	FE _{CO} stability ~66% after 4 h	[129]

Of note, F-CPC can maintain 97% of the initial current density and keep CO FE stable for 12 h. It turns out that the nanocage structure of F-CPC can generate an enhanced electrostatic field and increase the K^+ ion concentration, thereby lowering the thermodynamic energy barrier for CO_2RR . In another report [128], a fluorine interlayer doped carbon (FC) catalyst was obtained by the facile pyrolysis of the precursor's mixture, and the FC was able to reach the maximum FE for CO of 89.6% at -0.62 V. DFT calculations revealed that fluorine interlayer doping can activate neighbor carbon atom defects and contribute to the interaction of $COOH^*$ with activated carbon, which is considered as the rate-determining step for CO_2 -to-CO conversion. Likewise, S-doping can also result in higher spin density and charge delocalization owing to the dissimilar electronegativity of sulfur (2.58) and carbon (2.55), which are believed to enhance the electrocatalytic activity for CO_2RR . S-doped porous carbon nanosheets (CPSs) were prepared by the annealing of poly (4-styrene sulfonic acid-co-maleic acid) sodium salt at 800 °C under N_2 , which showed a higher CO_2RR current density (7.2 mA/cm²) than that of N-doped CPSs (CPSNs) (7.2 mA/cm²) [130]. The maximum FE for CO (FE_{CO}) and CH_4 on the CPSs was about (2.0% and 0.1%) at -0.99 V vs. RHE relative to the CPSNs (11.3% and 0.18%) due to S and/or N dopants, which stabilize the CO_2^- and $COOH^*$ intermediates that promote CO_2RR to CO and CH_4 . The durability studies showed that the CPSs maintained only 65% of their FE_{CO} (1.3%) after 2 h, while the CPSNs kept around 72.7% of their FE_{CO} (8%). With the relatively large difference between the electronegativity of B and C atoms, B-doping can induce charge polarization and make the carbon framework suitable for adsorbing CO_2 molecules. For instance, B-doped graphene (BG) was synthesized by catalyst by heating the graphene oxide and boric acid (1/5 wt ratio) at 900 °C under Ar, which showed higher CO_2RR activity with a current density of ~ 6 mA/cm² at 1.6 V than undoped graphene (~ 1.6 mA/cm²), and Bi (~ 2.4 mA/cm²) in 0.1 M $KHCO_3$ can reach an FE for formic acid of 66% at -1.4 V vs. SCE during CO_2RR [129]. BG mainly allowed the CO_2RR to formate with an FE of 66% at -1.4 V, which was substantially higher than Bi (FE of 20%). BG remains stable for 4 h without any significant loss in the CO_2RR activity. B-doped diamond (BDD) thin films were grown on Si(111) wafers by the microwave plasma-assisted chemical vapor deposition (MPVCD) method at 5 kW using B(OCH₃) (B-source) and acetone (C-source) with B/C (1/1 atomic ratio) [131]. BDD showed a current density of 0.3 mA/cm² at 2.2 V vs. Ag/AgCl in an electrolyte of methanol solution and tetrabutylammonium perchlorate (MeOH-TBAP). Moreover, BDD allowed the CO_2RR to produce formaldehyde, formic acid, and H_2 with a maximum FE of 74% at -1.7 V, 15% at -1.5 V, and 1.1% at <-1.7 V, respectively [131]. Interestingly, BDD revealed a higher CO_2RR activity with a greater FE for formaldehyde, formic acid, and H_2 in MeOH-TBAP electrolyte relative to water (0.1 M NaCl) and seawater, respectively. Notably, mono heteroatom-doped carbon-based catalysts for CO_2RR are rarely reported and are not studied enough (Table 3). Also, other reports did not systemically study the activity and durability as a function of dopant amount or in different electrolytes.

4.5. Binary Heteroatom-Doped Porous Carbon Materials

In consideration of the unsatisfying catalytic performance for single heteroatom-doped porous carbon materials, dual heteroatom co-doping may regulate the chemical properties in a wide range and bring great promise toward CO_2RR by virtue of the synergistic electronic interactions between different dopants. Table 4 shows a detailed comparison of the electrocatalytic performance of binary HA-PCs toward CO_2RR .

4.5.1. Nitrogen, Sulfur Co-Doped Porous Carbon Materials

Although there are few reports about the effect of sulfur dopants into porous carbon materials on CO_2RR , the co-doping of nitrogen and sulfur has been extensively investigated over the past few years [40,43,130,132–136]. Yang et al. reported N, S co-doped hierarchically porous carbon nanofiber (NSHCF) membranes as high-efficiency catalysts for electrochemical conversion of CO_2 to CO with 94% Faradaic efficiency at -0.7 V vs.

RHE [133]. In their synthesis, NSHCF900 was obtained by electrospinning the mixture of ZIF-8 nanoparticles, trithiocyanuric acid (TA), and polyacrylonitrile (PAN), followed by the carbonization at 900 °C in Ar (Figure 7A). In contrast, the NHCF900 without sulfur doping can only achieve a CO FE of 63% toward CO₂RR, highlighting the key role of S species in promoting electrochemical activity. Moreover, DFT calculations showed that the Gibbs free energy of *COOH on pyridinic N adjacent to the carbon-bonded S atom is effectively decreased compared to that on pure pyridinic N atoms (Figure 7B). This is likely due to the greater spin density and charge delocalization arising from S atom doping. Following this method, Li and coworkers synthesized N, S co-doped hierarchically porous carbon (NSHPC) by pyrolysis of glucosamine hydrochloride and thiocyanuric acid precursor using SiO₂ as a hard template, and they were able to obtain a maximum CO FE of 87.8% at −0.6 V vs. RHE [134]. The N, S co-doped high-surface-area carbon materials (SZ-HCN) were developed by one-step pyrolysis of N-containing polymer and S powder [136]. A partial current density of 5.2 mA/cm² at the overpotential of 0.490 V and a maximum CO FE of 93% at −0.6 V for CO₂RR was achieved on SZ-HCN, which is superior to those on the single N-doped carbon counterpart.

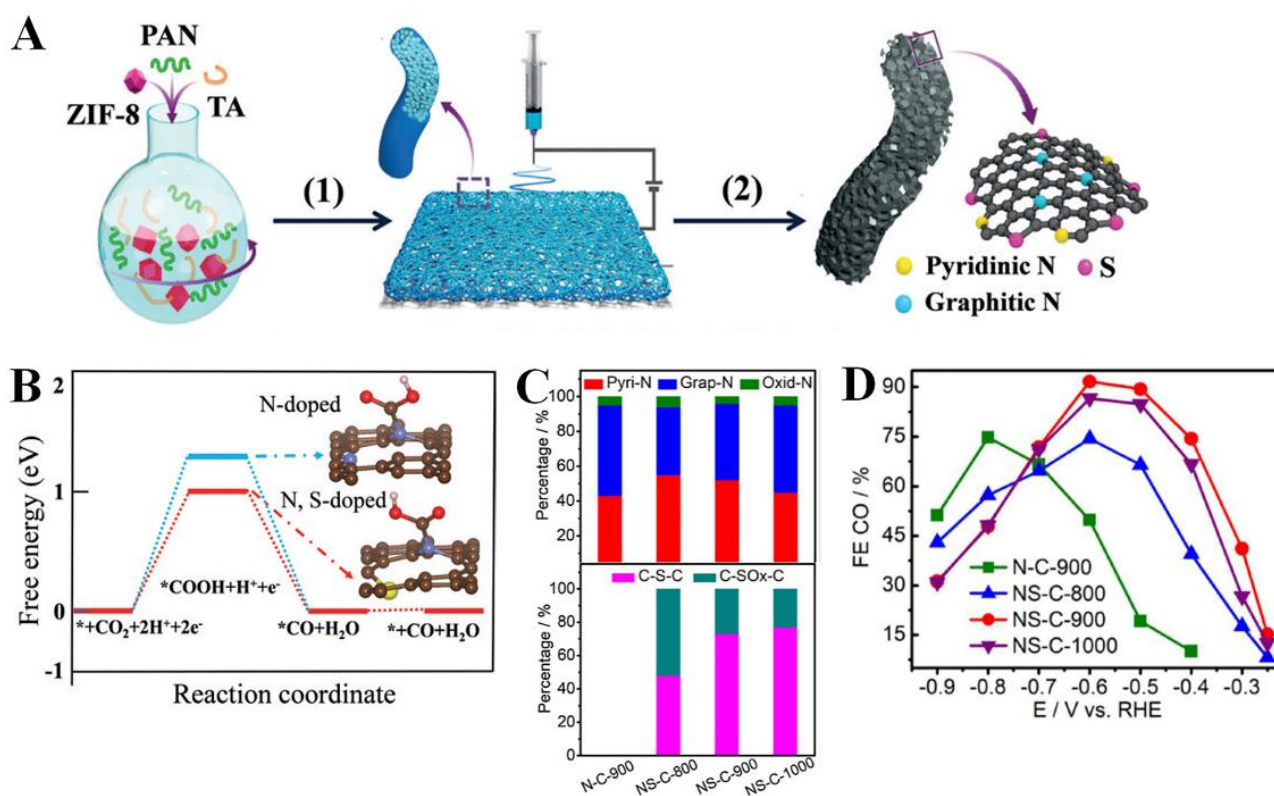


Figure 7. (A) Schematic illustration of the synthesis procedure of NSHCF. (B) The free energy diagram of CO₂-to-CO conversion on N-doped and N, S dual-doped graphene. Reproduced from [133]. Copyright 2018, John Wiley & Sons. (C) The calculated N, S percentages and (D) CO FE for N-C-900 and NS-C. Adapted from [40]. Copyright 2019, Elsevier.

In another study [40], Pan et al. concluded that sulfur addition could significantly boost the electrochemical activity and selectivity for CO₂RR of N-doped carbon catalysts. A layer-structured carbon nitride-templated pyrolysis strategy synthesized the N, S dual-doped carbon (NS-C) layers. Thiourea and citric acid were used as N, S sources and C sources, respectively. For comparison, the NS-C samples (denoted as NS-C-800, NS-C-900, and NS-C-1000) were prepared at different annealing temperatures of 800, 900, and 1000 °C to tune the doped N, S content, respectively. In addition, S-free N-C (denoted as N-C-900) layers were also obtained under identical synthesis conditions to those of NS-C-900,

except for replacing thiourea with urea. It is notable from Figure 7C that the S-doping is beneficial for forming highly active pyridinic N while suppressing graphitic N. The CO FE for each catalyst at various potentials is shown in Figure 7D. NS-C-900 can catalyze CO₂RR at a smaller overpotential but with a larger CO FE relative to N-C-900, showcasing the improved reactivity and selectivity after sulfur doping.

Furthermore, it was found that the catalytic activity of NS-C layers strongly depends on the annealing temperature, among which the NS-C annealed at 900 °C can yield the highest CO FE of 92%. This is mainly attributed to doped N and S species' optimal content and structure, which can expose more active sites and accelerate mass transport. DFT calculations were further employed to study the effect of sulfur doping on the inherent activity of various N dopants. They found that the distance between the S atom and pyridinic N is proportionally related to the enhancing effect of sulfur atoms. It was speculated that introducing S atoms can increase the spin density of N-C, which is more conducive to promoting electron transfer and COOH* adsorption, resulting in superior catalytic ability at a lower overpotential. Similarly, Li et al. revealed the relationship between the dispersion of S and N groups in porous carbon with the CO FE, verifying the enhancing effect of sulfur doping on highly active pyridinic N sites for CO₂RR [132].

4.5.2. Nitrogen, Phosphorus Co-Doped Porous Carbon Materials

In view of the larger difference between heteroatom P and N in electronegativity, dual-doping into porous carbon materials provides more options to boost the electrocatalytic performance toward CO₂RR [137–140]. Chen et al. fabricated N, P co-doped carbon materials (NPCM-1000) using aniline monomer and phytic acid as nitrogen, carbon, and phosphorus sources via one-pot pyrolysis at 1000 °C (Figure 8A). As a reference, single N-doped carbon materials (NCM-1000) were synthesized by replacing phytic acid with HCl. The NPCM-1000 exhibits a similar structure to NCM-1000 but with a higher surface area, pyridine N content, and defects, as revealed by TEM, N₂ adsorption–desorption measurement, X-ray photoelectron spectroscopy, and Raman spectra, respectively. The electrochemical tests were conducted using a standard three-electrode system using a CO₂-saturated 0.5 M NaHCO₃ solution. As expected, the NPCM-1000 exhibits a higher onset potential (−0.38 V) than NCM-1000 (−0.59 V) (Figure 8B). The CO FEs at various potentials of NPCM-1000 and NCM-1000 are displayed in Figure 8C, in which the maximum FE for NPCM-1000 and NCM-1000 is 92% and 14% at −0.55 V, respectively. Moreover, NPCM-1000 shows much higher partial current densities of CO (j_{co}) than NCM-1000 (Figure 8D). The Tafel curve is generally used to describe the reaction kinetics of CO₂RR. The Tafel slope of 122 mV/dec for NPCM-1000 implies the formation of COOH* is the rate-determining step, while for NCM-1000 it is the CO₂ molecular adsorption and desorption (Figure 8E). Based on DFT calculations, the N, P co-doping can synergistically promote the formation of COOH*. Furthermore, the reaction barrier of CO₂ activation can be more effectively reduced for NPCM-1000 than that for NCM-1000, as calculated from Figure 8F,G. Recently, Liang and co-workers demonstrated a porous N, P dual-doped carbon nanosheet catalyst for CO₂RR which can attain a high CO FE of 88% and good stability for 27 h at a low overpotential [140]. In addition, they found that the introduction of P can adjust the electronic structure of pyridinic N to hinder the adsorption of *H and contribute to the higher selectivity of CO₂-to-CO.

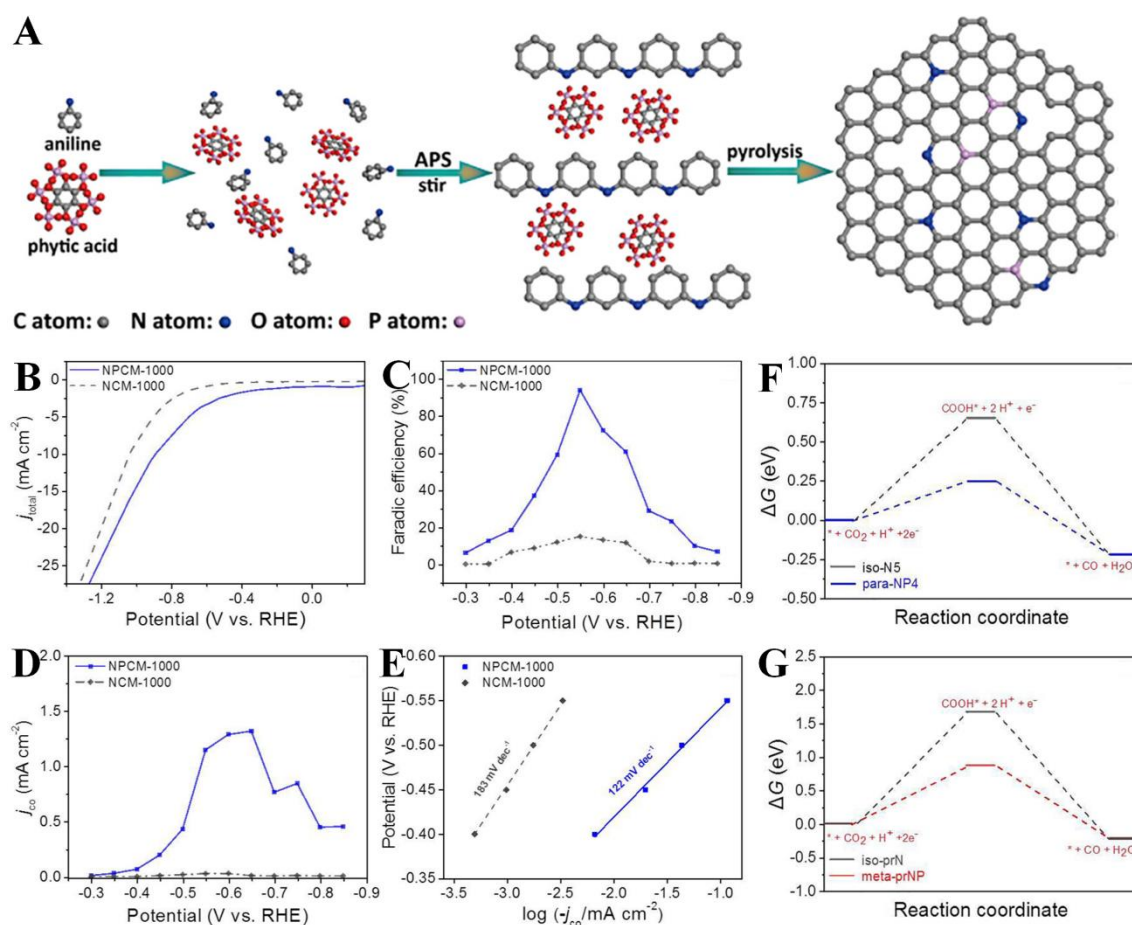


Figure 8. (A) Schematic illustration of synthesis process of NPCM. (B) Linear sweep voltammetry curves of NPCM-1000 and NCM-1000 in CO_2 saturated 0.5 M KHCO_3 solution with a sweeping rate of 2 mV/s. (C) The CO FEs at various potentials, (D) j_{CO} , and (E) Tafel plots for NPCM-1000 and NCM-1000, respectively. The Gibbs free energies changes for (F) iso-N5, para-NP4 and (G) iso-prN, meta-prNP. Reproduced from [140]. Copyright 2022, American Chemical Society.

4.5.3. Nitrogen, Boron Co-Doped Porous Carbon Materials

Since N atoms have a larger electronegativity and B atoms have a smaller electronegativity than C atoms, N/B co-dopants may modulate the electronic structure and create an unexpected effect on CO_2RR [33]. As reported previously [141], B, N co-doped nanodiamond (BND) was an efficient and stable electrocatalyst for CO_2RR to ethanol. BND revealed a high FE of 93.2% at -1.0 V vs. RHE due to the synergistic effect of B and N co-dopants. Then, various HA-PCs co-doped with B and N were reported for the CO_2RR [142,143]. Zhao's group has reported the integrated design of a N, B co-doped three-dimensional hierarchical porous carbon network with a high doping level by a salt-sugar method [144].

The as-obtained catalyst displays a high CO_2 -to-CO FE of 83% at a low overpotential of 290 mV and good stability over 20 h. Based on the physical and electrochemical characterization, the superior activity and selectivity are first attributed to the unique porous structure, including macropores, mesopores, and micropores, which can offer larger surface areas and more active sites for CO_2 adsorption. Moreover, the N-doping can accelerate the conversion of CO_2 into the CO_2^* intermediate, while the B atoms can facilitate the capture of CO_2 by bonding to the O atoms of the CO_2^* intermediate, and then the conversion of COOH^* into CO^* . B, N co-doped mesoporous carbon (BNMC) was synthesized through carbonization of the mixed precursors using glucose as the carbon source, urea and dicyandiamide as the nitrogen source, and boric acid as the boron source along with silica as a template (Figure 9A) [142]. The as-synthesized BNMC annealed at 1000°C

(BNMC-1000) possesses a porous surface, as seen from the scanning electron microscopy (SEM) image in Figure 9B. The TEM image of BNMC-1000 reveals the rich mesopores with an average diameter of 25 nm (Figure 9C). For comparison, control experiments of BNC-1000 without mesopores, NMC-1000 without B-doping, and BMC-1000 without N-doping were conducted to explore the effect of the porous structure and heteroatom doping. As shown in Figure 9D,E, the BNC-1000 reveals a very low current density and CO FE compared with NMC-1000 and BNMC-1000, indicating the critical role of the mesoporous structure in enhancing CO₂RR. Furthermore, the current density and CO FE of BNMC-1000 is larger than those of NMC-1000, demonstrating that the N, B dual-doping contributes to improving CO₂RR relative to single N-doping. They also confirmed that BMC-1000 could reduce CO₂ to formic acid with a different electrochemical selectivity from NMC-1000 and BNMC-1000. The Tafel slope of BNMC-1000 was calculated to be 128 mV/dec, which is smaller than that of NMC-1000 (141 mV/dec), indicating the favorable reaction kinetics on BNMC-1000 through N, B dual-doping (Figure 9F). DFT calculations reveal that the coupling effect between N and B atoms can tune the projected density of states of adjacent carbon active sites, thereby generating an optimal adsorbed energy of *COOH and *CO on the carbon surface.

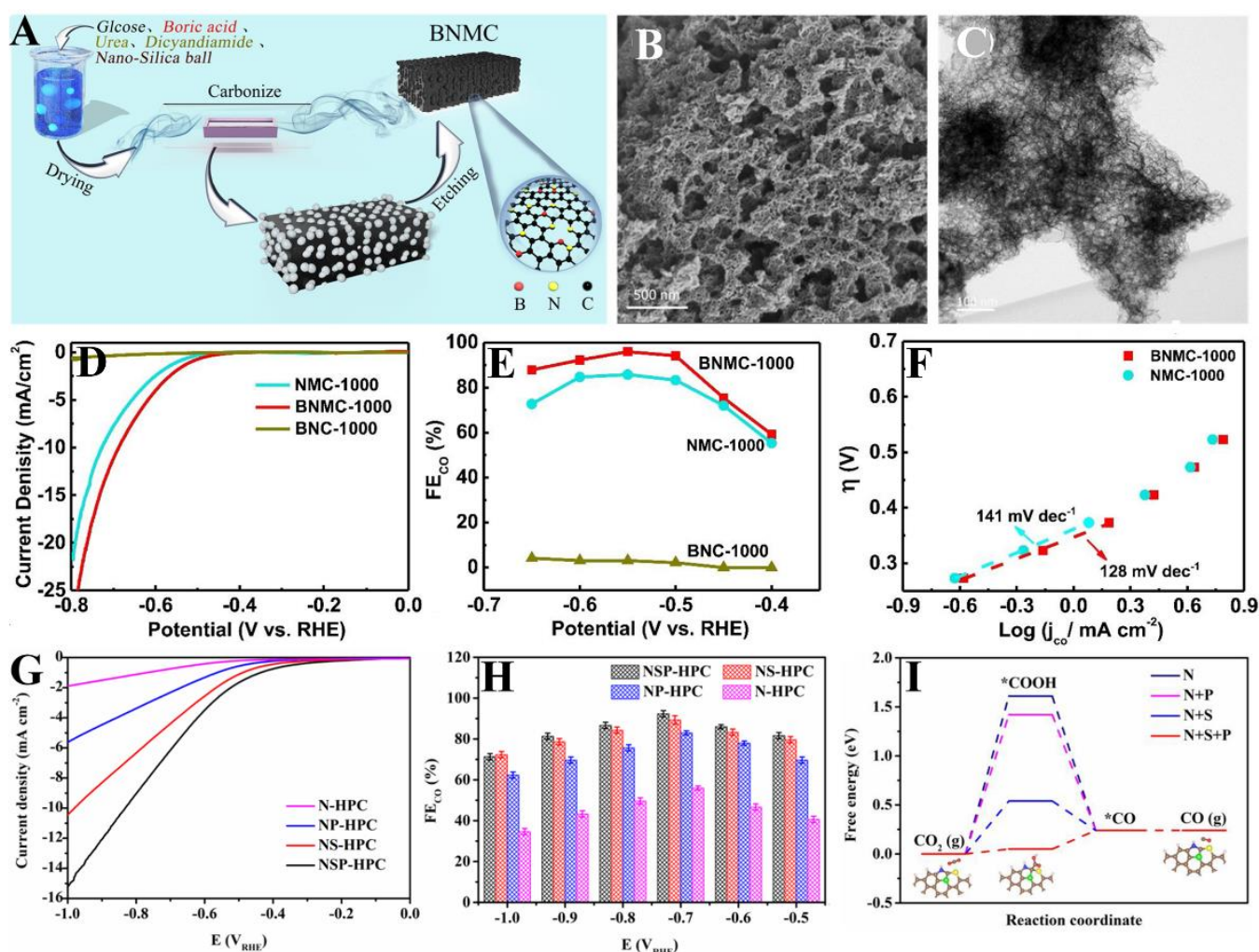


Figure 9. (A) Schematic illustration of the synthesis of BNMC. (B) SEM and (C) TEM of BNMC. (D) LSV curves in CO₂-saturated 0.1 M KHCO₃. (E) CO FE at different potentials from −0.4 to −0.65 V. (F) Tafel plots of NMC-1000 and BNMC-1000. Adapted from [142]. Copyright 2021, Elsevier. (G) LSV curves, (H) CO FEs at different potentials, and (I) free energy diagrams of CO₂RR for all catalysts. Reproduced from [145]. Copyright 2021, Elsevier.

Table 4. Comparison of electrocatalytic performance of binary and ternary HA-PCs toward CO₂RR.

Electrocatalysts	Synthetic Method	Electrolyte	Main Products	Potential of FE_{max} (vs. RHE)	FE_{max} (%) / j_{CO} (mA cm ⁻²)	Durability	Refs.
Binary HA-PCs							
CPSN	The carbonization of poly(4-styrenesulfonic acid-co-maleic acid) sodium salt at 800 °C, followed by impregnation with urea-saturated solution and holding at 800 °C in N ₂ for 30 min	0.1 M KHCO ₃	CO CH ₄	-0.99	11.3, 0.18% / ~-4 mA cm ⁻²	FE _{CO} stability ~8, 0.126% after 27, 2 h	[130]
NSHCF900	The carbonization of polymer nanofiber at 900 °C in Ar	0.1 M KHCO ₃	CO	-0.7	94% / ~-103 mA cm ⁻²	FE _{CO} stability ~93% after 36 h	[133]
NS-C	The calcination of citric acid and thiourea at 550 °C for 2 h under Ar	0.1 M KHCO ₃	CO	0.49 (over-potential)	92% / ~-2.63 mA cm ⁻²	FE _{CO} stability ~91% after 20 h	[40]
NS-CNSs-1000	Two-step pyrolysis of the mixture of iron-oleate, Na ₂ SO ₄ and urea and acid etching	0.5 M KHCO ₃	CO	-0.55	85.4% / ~-2.5 mA cm ⁻²	FE _{CO} stability over 80% after 20 h	[43]
NSHPC	The pyrolysis of glucosamine hydrochloride and thiocyanuric acid precursor using SiO ₂ as hard templates	0.1 M KHCO ₃	CO	-0.6	87.8% / ~-2.2 mA cm ⁻²	FE _{CO} stability ~80% after 10 h	[134]
SZ-HCN	One-step pyrolysis of N-containing polymer and S powder	0.1 M KHCO ₃	CO	-0.6	93% / ~-5.2 mA cm ⁻²	FE _{CO} stability ~90% after 20 h	[136]
BAX-TU-20	High-temperature treatment of commercial wood-based carbon impregnated with thiourea	0.1 M KHCO ₃	CO CH ₄	0.67	29, 0.27% / ~-1.5 mA cm ⁻²	FE _{CO} stability ~22.5, 0.25% after 40, 50 h	[132]
NPC-900-2	Pyrolysis-controlled sacrificial templating approach using citric acid, melamine and NH ₃ , and phytic acid as carbon, nitrogen, and phosphorous source, respectively	0.5 M KHCO ₃	CO	-0.41	88% / ~-1.71 mA cm ⁻²	FE _{CO} stability ~80% after 27 h	[140]
NPCM-1000	One-pot synthesis by using aniline monomer and phytic acid as nitrogen, carbon, and phosphorus source	0.5 M NaHCO ₃	CO	-0.55	92% / ~-1.25 mA cm ⁻²	FE _{CO} stability ~75% after 24 h	[139]
MPC-1000	Pyrolysis of vitamin B ₁₂ in NaCl assembly-enclosed nanoreactors	0.1 M KHCO ₃	CO	-0.7	62% / ~-3.1 mA cm ⁻²	FE _{CO} stability ~60% after 20 h	[137]
N, P-FC	One-step soft-template pyrolysis method by using phytic acid as P source, dicyandiamide as N source, and polyethylene glycol as soft template	0.5 M NaHCO ₃	CO	-0.52	83.3% / ~-8.52 mA cm ⁻²	FE _{CO} stability ~80% after 12.5 h	[138]
NBPC	Liquid nitrogen-assisted freeze-drying of the NaCl-glucose solution containing carbon, nitrogen, and boron precursors and two-stage solid pyrolysis	0.5 M KHCO ₃	CO	-0.4	83% / ~-0.5 mA cm ⁻²	FE _{CO} stability ~80% after 20 h	[144]
BND3	The deposition of BND film on Si substrate using hot filament chemical vapor deposition method with a gas mixture of CH ₄ /B ₂ H ₆ /N ₂ /H ₂	0.1 M NaHCO ₃	CH ₃ CH ₂ OH CH ₃ OH HCOO ⁻	-1.0	93.2% / ~-0.5 mA cm ⁻²	FE _{CO} stability ~93.2% after 48 h	[141]

Table 4. Cont.

Electrocatalysts	Synthetic Method	Electrolyte	Main Products	Potential of FE_{max} (vs. RHE)	FE_{max} (%) / j_{CO} ($mA cm^{-2}$)	Durability	Refs.
BNMC-1000	The carbonization of a precursor containing urea, dicyandiamide, glucose, and boric acid along with silica as templates	0.1 M $KHCO_3$	CO	−0.55	95% / \sim −2.7 $mA cm^{-2}$	FE_{CO} stability \sim 90% after 10 h	[142]
Ternary HA-PCs							
NSP-HPC	A H_2SO_4 - H_3PO_4 binary-acids activation method	0.5 M $KHCO_3$	CO	−0.7, −1	92, 98.5% / \sim −5.2, −186 $mA cm^{-2}$	FE_{CO} stability \sim 91, 94% after 50 h	[145]
LC-3	The carbonization of the mixture of lignin, urea, melamine, NaCl, and $ZnCl_2$ at 1000 °C for 2 h in Ar, followed by impregnating in HCl for 24 h	0.1 M $KHCO_3$	CO	−0.6	95.9% / \sim −1.98 $mA cm^{-2}$	FE_{CO} stability \sim 95.9% after 18 h	[135]

4.6. Ternary Heteroatom-Doped Porous Carbon Materials

Introducing multiple heteroatoms with different electronegativities and sizes to porous carbon materials can modify the local electronic properties, thereby boosting the electrochemical CO_2RR . Table 4 shows a detailed comparison of the electrocatalytic performance of ternary HA-PCs toward CO_2RR . Yang et al. presented a facile synthesis of N, P, S ternary heteroatom-doped carbon (NSP-HPC) via the H_2SO_4 - H_3PO_4 binary-acids activation method [145]. The dual heteroatom-doped NS-HPC, NP-HPC, and single-doped N-HPC were also prepared as a control. In a conventional H-cell, NSP-HPC exhibits the lowest onset potential of −0.38 V among the four samples, which corresponds to a smaller overpotential of 270 mV (Figure 9G). Moreover, NSP-HPC demonstrates the highest CO FE among the control samples at various potentials (Figure 9H). The maximum CO FE for NSP-HPC is 92%, achieved at −0.7 V, while that for NP-HPC, NS-HPC, and N-HPC is 83%, 90%, and 56%, respectively. More importantly, the current density and CO FE of NSP-HPC can keep constant for 50 h at −0.7 V, reflecting its robust stability. In situ Raman spectroscopy reveals that *COOH is the key intermediate in CO_2 -to-CO conversion. Based on the DFT calculations, the free energy diagrams of CO_2RR for each catalyst are given in Figure 9I. During the CO_2 -to-CO conversion, the free energy barrier of *COOH is 1.61 eV for N-doped carbon. Once P or S atoms are introduced, the free energy barrier decreases to 1.42 and 0.54 eV, respectively. The N, S, and P doping reveals the lowest *COOH formation energy of 0.05 eV, indicating that the synergistic coupling effect among multiple heteroatoms could benefit the enhanced CO_2RR . Furthermore, the well-defined hierarchically porous structure of NSP-HPC also plays a key role in improving the CO_2RR activity.

5. Conclusions and Outlook

In summary, this review discussed the controlled synthesis and emphasized the rational synthesis of heteroatom (i.e., N, S, O, F, or B)-doped porous carbon nanostructures (HA-PCs) for the CO_2RR . This includes the CO_2RR fundamental pathways and engineering methods of HA-PC nanostructures. The effects of dopants (individually or mixed) on the CO_2RR activity and durability were reported.

The Faradaic efficiency (FE), overpotential (η), partial current density (j), durability, energy efficiency (E_{eff}), and turnover frequency (TOF) are the main factors that determine the CO_2RR activity of HA-PCs.

There are a few methods for the rational synthesizing of HA-PC nanostructures: template-based, activation, element-doping, and direct annealing of biomass-based resources, which vary in their productivity for tailoring the porosity (i.e., pore-volume, pore order, and pore size), surface area, and structure of HA-PCs. Hard template methods

(Zn-based, Mg-based, Ca-based, and Si-based) are extensively studied for HA-PCs. This is due to their ability to produce uniform porous morphologies with well-controlled porosity and surface area, but their multiple reaction steps and use of hazardous chemicals for etching templates remain a grand challenge. However, the Zn-based template is the most preferred among hard templates because Zn is inexpensive, earth-abundant, and can be easily prepared in high yield and evaporate during annealing without additional etching steps. New templates such as melamine, dry ice, and MXene have also allowed the synthesis of HA-PCs, but they have rarely been reported. Soft templates including ionic/nonionic copolymers (i.e., F127 and cetrimonium chloride) and ionic liquids (i.e., Gemini-type) are also used for the preparation of HA-PCs, but they cannot produce uniform porous structures with a high surface area and they are usually accompanied with other methods.

Deriving HA-PCs from biomass is among the most promising approaches due to the low-cost and natural abundance of biomass waste; also, the unique structures and composition of biomass wastes drive the production of HA-PCs with well-defined porosity and composition under ambient conditions that meet the sustainability requirements. Using melamine is highly promising as it allows integration of high N content and constructer carbon-nitride over HA-PCs during carbonization at a temperature above 500 °C. MOF-derived HA-PCs are also studied significantly, but their high cost and multiple/complicated reaction steps remain a significant challenge. Moreover, the use of activators is needed to enhance the surface area and porosity.

Various HA-PC nanostructures have been prepared using multiple methods for CO₂RR, which varied in their performance (Tables 3 and 4). Notably, KHCO₃ and NaHCO₃ are the main electrolytes used for HA-PCs, and NaClO₄ electrolytes were rarely reported; furthermore, CO is the main CO₂RR product, and other products such as CH₄, HCOOH, C₂H₅OH, and CH₃OH were rarely found, which implies the selectivity of HA-PCs for producing CO.

The biomass-derived HA-PCs are the most promising for practical applications. Chlorine-promoted N/S co-doped PCs (LC-3) formed from annealing of lignin, urea, melamine, NaCl, and ZnCl₂ at 100 °C and impregnating in HCl revealed an FE of 95.9% [134] and N/B-doped porous carbon (BNMC-1000) showed an FE of 95% [142], and N-doped porous carbon from calcination of ZIF-8 (NC1100) showed an FE of 95.4% [107]. N-doped PCs are the most reported and most active compared to other HAs dopants, and they are the most active for CO₂RR. The highest active HA-PCs are N-doped porous carbon (NPC-1000) formed using annealing of Zn-MOF-74 and with melamine at 1000 °C showing an FE of 98.4% [119] and N-doped porous carbon (N/C-Cl-1100) obtained from halogen-assisted annealing of ZIF-8 with KCl at 1100 °C revealing an FE of 99.5% [117]. This is due to their porosity and abundance of N-species (i.e., pyridinic-N and graphitic-N). B/N-doped nanodiamond (BND) produced only ethanol with an FE of 93.2% [141]. Despite the noticed progress in HA-PC catalysts for CO₂RR, they are still far from being useful for large-scale applications, so various perspectives and challenges should be addressed:

- The current preparation approaches of heteroatom-doped porous carbon-based nanocatalysts involve multiple reaction steps, energy consumption, and hazardous reagents, making them impractical. Thus, they should be prepared using green materials under ambient conditions to meet sustainability requirements.
- Using biomass wastes is a promising approach to synthesizing HA-PCs with tunable porosity and surface area under ambient conditions; however, they are rarely reported for CO₂RR.
- The CO₂RR performance of HA-PCs is mainly measured in CO₃-based electrolytes, so other organic, ionic liquid, and hybrid electrolytes should be studied to produce liquid products other than CO. Moreover, the effect of electrolytes and cell design on the CO₂RR of HA-PCs has not yet been reported.
- Integration of HA-PCs with other materials such as carbon nitride [1,146–148], MXenes [23,149–151], carboxylated carbon/graphene [152,153], and graphdiyne [41] can

enhance their CO₂RR owing to their rich electron density, unique physicochemical properties, and catalytic/photocatalytic merits. Using HA-PCs with 3D porous multi-metallic nanocrystals (i.e., cages, branched, dendrites, and yolk-shell) can improve the CO₂RR selectivity.

- Computational studies could be conducted with experimental studies to allow the synthesis of novel HA-PCs and to examine their CO₂RR activity, mechanism, and pathways.

Author Contributions: All authors contributed equally to this work. Collecting the data and writing—original draft preparation, Q.L. and K.E.; collecting data, writing, and editing, K.E. and W.L.; supervision and project administration, W.L. All authors have read and agreed to the published version of the manuscript.

Funding: This work was financially funded by project ZR2020QB070 supported by the Shandong Provincial Natural Science Foundation, the Introduction and Cultivation Plan of Young Innovative Talents in Colleges and Universities of Shandong Province, Open Project Program for State Key Laboratory Base of Ecochemical Engineering (Qingdao University of Science & Technology) (No. STHG 2002).

Institutional Review Board Statement: Not applicable.

Informed Consent Statement: Not applicable.

Data Availability Statement: The data presented in this study are available on request from the corresponding author.

Conflicts of Interest: The authors declare no conflict of interest.

References

1. Lu, Q.; Eid, K.; Li, W.; Abdullah, A.M.; Xu, G.; Varma, R.S. Engineering graphitic carbon nitride (gC₃N₄) for catalytic reduction of CO₂ to fuels and chemicals: Strategy and mechanism. *Green Chem.* **2021**, *23*, 5394–5428. [[CrossRef](#)]
2. Eid, K.; Sliem, M.H.; Eldesoky, A.S.; Al-Kandari, H.; Abdullah, A.M. Rational synthesis of one-dimensional carbon nitride-based nanofibers atomically doped with Au/Pd for efficient carbon monoxide oxidation. *Int. J. Hydrog. Energy* **2019**, *44*, 17943–17953. [[CrossRef](#)]
3. Eid, K.; Sliem, M.H.; Abdullah, A.M. Unraveling template-free fabrication of carbon nitride nanorods codoped with Pt and Pd for efficient electrochemical and photoelectrochemical carbon monoxide oxidation at room temperature. *Nanoscale* **2019**, *11*, 11755–11764. [[CrossRef](#)]
4. Eid, K.; Sliem, M.H.; Al-Kandari, H.; Sharaf, M.A.; Abdullah, A.M. Rational synthesis of porous graphitic-like carbon nitride nanotubes codoped with Au and Pd as an efficient catalyst for carbon monoxide oxidation. *Langmuir* **2019**, *35*, 3421–3431. [[CrossRef](#)]
5. Lu, Q.; Li, J.; Eid, K.; Gu, X.; Wan, Z.; Li, W.; Al-Hajri, R.S.; Abdullah, A.M. Facile One-step Aqueous-phase Synthesis of Porous PtBi Nanosponges for Efficient Electrochemical Methanol Oxidation with a High CO Tolerance. *J. Electroanal. Chem.* **2022**, *916*, 116361. [[CrossRef](#)]
6. Eid, K.; Abdullah, A.M. Porous Ternary Pt-based Branched Nanostructures for Electrocatalytic Oxygen Reduction. *Electrochem. Commun.* **2022**, *136*, 107237. [[CrossRef](#)]
7. Ahsan, M.A.; He, T.; Eid, K.; Abdullah, A.M.; Sanad, M.F.; Aldalbahi, A.; Alvarado-Tenorio, B.; Du, A.; Puente Santiago, A.R.; Noveron, J.C. Controlling the Interfacial Charge Polarization of MOF-Derived 0D–2D vdW Architectures as a Unique Strategy for Bifunctional Oxygen Electrocatalysis. *ACS Appl. Mater. Interfaces* **2022**, *14*, 3919–3929. [[CrossRef](#)]
8. Wang, H.; Yin, S.; Eid, K.; Li, Y.; Xu, Y.; Li, X.; Xue, H.; Wang, L. Fabrication of mesoporous cage-bell Pt nanoarchitectonics as efficient catalyst for oxygen reduction reaction. *ACS Sustain. Chem. Eng.* **2018**, *6*, 11768–11774. [[CrossRef](#)]
9. Wu, F.; Eid, K.; Abdullah, A.M.; Niu, W.; Wang, C.; Lan, Y.; Elzatahry, A.A.; Xu, G. Unveiling one-pot template-free fabrication of exquisite multidimensional PtNi multicube nanoarchitectonics for the efficient electrochemical oxidation of ethanol and methanol with a great tolerance for CO. *ACS Appl. Mater. Interfaces* **2020**, *12*, 31309–31318. [[CrossRef](#)]
10. Logeshwaran, N.; Panneerselvam, I.R.; Ramakrishnan, S.; Kumar, R.S.; Kim, A.R.; Wang, Y.; Yoo, D.J. Quasihexagonal Platinum Nanodendrites Decorated over CoS₂-N-Doped Reduced Graphene Oxide for Electro-Oxidation of C1-, C2-, and C3-Type Alcohols. *Adv. Sci.* **2022**, *9*, 2105344. [[CrossRef](#)]
11. Ghanem, A.; Mandor, M.A.; El-Nagar, R.; Eid, K. Atomic and Molecular Functionalization of Graphitic Carbon Nitride for Solar Cell Applications. In *Carbon Nitride Nanostructures for Sustainable Energy Production and Environmental Remediation*; RSC: London, UK, 2021; pp. 221–261.
12. Chen, L.; Xu, C.; Qin, Y.; He, X.; Bian, H.; Xu, G.; Niu, L.; Song, Q. An Inverted Perovskite Solar Cell with Good Comprehensive Performance Realized by Reducing the Concentration of Precursors. *Nanomaterials* **2022**, *12*, 1736. [[CrossRef](#)] [[PubMed](#)]
13. Eid, K.; Sliem, M.H.; Abdullah, A.M. Tailoring the defects of sub-100 nm multipodal titanium nitride/oxytitanium nitride nanotubes for efficient water splitting performance. *Nanoscale Adv.* **2021**, *3*, 5016–5026. [[CrossRef](#)]

14. Eid, K.; Soliman, K.A.; Abdulmalik, D.; Mitoraj, D.; Sleim, M.H.; Liedke, M.O.; El-Sayed, H.A.; AlJaber, A.S.; Al-Qaradawi, I.Y.; Reyes, O.M. Tailored fabrication of iridium nanoparticle-sensitized titanium oxynitride nanotubes for solar-driven water splitting: Experimental insights on the photocatalytic–activity–defects relationship. *Catal. Sci. Technol.* **2020**, *10*, 801–809. [[CrossRef](#)]
15. Ahmad, Y.H.; Eid, K.A.; AlQaradawi, S.Y.; Allam, N.K. Highly active, durable and pH-universal hybrid oxide nanocrystals for efficient oxygen evolution. *Sustain. Energy Fuels* **2017**, *1*, 1123–1129. [[CrossRef](#)]
16. Ipadeola, A.K.; Lebechi, A.K.; Gaolatlhe, L.; Haruna, A.B.; Chitt, M.; Eid, K.; Abdullah, A.M.; Ozoemena, K.I. Porous High-Entropy Alloys as Efficient Electrocatalysts for Water-Splitting Reactions. *Electrochem. Commun.* **2022**, *136*, 107207. [[CrossRef](#)]
17. Ipadeola, A.K.; Haruna, A.B.; Gaolatlhe, L.; Lebechi, A.K.; Meng, J.; Pang, Q.; Eid, K.; Abdullah, A.M.; Ozoemena, K.I. Efforts at Enhancing Bifunctional Electrocatalysis and Related Events for Rechargeable Zinc-Air Batteries. *ChemElectroChem* **2021**, *8*, 3998–4018. [[CrossRef](#)]
18. Logeshwaran, N.; Ramakrishnan, S.; Chandrasekaran, S.S.; Vinothkannan, M.; Kim, A.R.; Sengodan, S.; Velusamy, D.B.; Varadhan, P.; He, J.-H.; Yoo, D.J. An efficient and durable trifunctional electrocatalyst for zinc–air batteries driven overall water splitting. *Appl. Catal. B* **2021**, *297*, 120405. [[CrossRef](#)]
19. Soliman, A.; AlAmoodi, N.; Karanikolos, G.N.; Doumanidis, C.C.; Polychronopoulou, K. A review on new 3-D printed materials' geometries for catalysis and adsorption: Paradigms from reforming reactions and CO₂ capture. *Nanomaterials* **2020**, *10*, 2198. [[CrossRef](#)]
20. Wan, Y.; Miao, Y.; Qiu, T.; Kong, D.; Wu, Y.; Zhang, Q.; Shi, J.; Zhong, R.; Zou, R. Tailoring Amine-Functionalized Ti-MOFs via a Mixed Ligands Strategy for High-Efficiency CO₂ Capture. *Nanomaterials* **2021**, *11*, 3348. [[CrossRef](#)]
21. Modak, A.; Bhanja, P.; Dutta, S.; Chowdhury, B.; Bhaumik, A. Catalytic reduction of CO₂ into fuels and fine chemicals. *Green Chem.* **2020**, *22*, 4002–4033. [[CrossRef](#)]
22. Guzmán, H.; Russo, N.; Hernández, S. CO₂ valorisation towards alcohols by Cu-based electrocatalysts: Challenges and perspectives. *Green Chem.* **2021**, *23*, 1896–1920. [[CrossRef](#)]
23. Eid, K.; Lu, Q.; Abdel-Azeim, S.; Soliman, A.; Abdullah, A.M.; Abdelgwad, A.M.; Forbes, R.P.; Ozoemena, K.I.; Varma, R.S.; Shibl, M.F. Highly exfoliated Ti₃C₂T_x MXene nanosheets atomically doped with Cu for efficient electrochemical CO₂ reduction: An experimental and theoretical study. *J. Mater. Chem. A* **2022**, *10*, 1965–1975. [[CrossRef](#)]
24. Bian, J.; Zhang, Z.; Feng, J.; Thangamuthu, M.; Yang, F.; Sun, L.; Li, Z.; Qu, Y.; Tang, D.; Lin, Z. Energy Platform for Directed Charge Transfer in the Cascade Z-Scheme Heterojunction: CO₂ Photoreduction without a Cocatalyst. *Angew. Chem. Int. Ed.* **2021**, *60*, 20906–20914. [[CrossRef](#)] [[PubMed](#)]
25. Ren, X.; Liu, S.; Li, H.; Ding, J.; Liu, L.; Kuang, Z.; Li, L.; Yang, H.; Bai, F.; Huang, Y. Electron-withdrawing functional ligand promotes CO₂ reduction catalysis in single atom catalyst. *Sci. China Chem.* **2020**, *63*, 1727–1733. [[CrossRef](#)]
26. Zhu, D.D.; Liu, J.L.; Qiao, S.Z. Recent advances in inorganic heterogeneous electrocatalysts for reduction of carbon dioxide. *Adv. Mater.* **2016**, *28*, 3423–3452. [[CrossRef](#)] [[PubMed](#)]
27. Song, Q.-W.; Zhou, Z.-H.; He, L.-N. Efficient, selective and sustainable catalysis of carbon dioxide. *Green Chem.* **2017**, *19*, 3707–3728. [[CrossRef](#)]
28. Franco, F.; Rettenmaier, C.; Jeon, H.S.; Roldan Cuenya, B. Transition metal-based catalysts for the electrochemical CO₂ reduction: From atoms and molecules to nanostructured materials. *Chem. Soc. Rev.* **2020**, *49*, 6884–6946. [[CrossRef](#)]
29. Wu, Y.; Cao, S.; Hou, J.; Li, Z.; Zhang, B.; Zhai, P.; Zhang, Y.; Sun, L. Rational Design of Nanocatalysts with Nonmetal Species Modification for Electrochemical CO₂ Reduction. *Adv. Energy Mater.* **2020**, *10*, 2000588. [[CrossRef](#)]
30. Eid, K.; Abdullah, A.M. Data on the catalytic CO oxidation and CO₂ reduction durability on gC₃N₄ nanotubes Co-doped atomically with Pd and Cu. *Data Br.* **2019**, *26*, 104495. [[CrossRef](#)]
31. Eid, K.; Sliem, M.H.; Jlassi, K.; Eldesoky, A.S.; Abdo, G.G.; Al-Qaradawi, S.Y.; Sharaf, M.A.; Abdullah, A.M.; Elzatahry, A.A. Precise fabrication of porous one-dimensional gC₃N₄ nanotubes doped with Pd and Cu atoms for efficient CO oxidation and CO₂ reduction. *Inorg. Chem. Commun.* **2019**, *107*, 107460. [[CrossRef](#)]
32. Liu, Y.; Zhao, G.-J.; Zhang, J.-X.; Bai, F.-Q.; Zhang, H.-X. First-principles investigation on the interfacial interaction and electronic structure of BiVO₄/WO₃ heterostructure semiconductor material. *Appl. Surf. Sci.* **2021**, *549*, 149309. [[CrossRef](#)]
33. Cui, H.; Guo, Y.; Guo, L.; Wang, L.; Zhou, Z.; Peng, Z. Heteroatom-doped carbon materials and their composites as electrocatalysts for CO₂ reduction. *J. Mater. Chem. A* **2018**, *6*, 18782–18793. [[CrossRef](#)]
34. Zhu, Y.; Yang, X.; Peng, C.; Priest, C.; Mei, Y.; Wu, G. Carbon-Supported Single Metal Site Catalysts for Electrochemical CO₂ Reduction to CO and Beyond. *Small* **2021**, *17*, 2005148. [[CrossRef](#)] [[PubMed](#)]
35. Liang, M.; Liu, Y.; Zhang, J.; Wang, F.; Miao, Z.; Diao, L.; Mu, J.; Zhou, J.; Zhuo, S. Understanding the role of metal and N species in M@NC catalysts for electrochemical CO₂ reduction reaction. *Appl. Catal. B* **2022**, *306*, 121115. [[CrossRef](#)]
36. Zhang, W.; Jia, B.; Liu, X.; Ma, T. Surface and interface chemistry in metal-free electrocatalysts for electrochemical CO₂ reduction. *SmartMat* **2022**, *3*, 5–34. [[CrossRef](#)]
37. Lu, Q.; Chen, C.; Di, Q.; Liu, W.; Sun, X.; Tuo, Y.; Zhou, Y.; Pan, Y.; Feng, X.; Li, L. Dual Role of Pyridinic-N Doping in Carbon-Coated Ni Nanoparticles for Highly Efficient Electrochemical CO₂ Reduction to CO over a Wide Potential Range. *ACS Catal.* **2022**, *12*, 1364–1374. [[CrossRef](#)]
38. Wang, Q.; Lei, Y.; Wang, D.; Li, Y. Defect engineering in earth-abundant electrocatalysts for CO₂ and N₂ reduction. *Energy Environ. Sci.* **2019**, *12*, 1730–1750. [[CrossRef](#)]
39. Liu, A.; Gao, M.; Ren, X.; Meng, F.; Yang, Y.; Gao, L.; Yang, Q.; Ma, T. Current progress in electrocatalytic carbon dioxide reduction to fuels on heterogeneous catalysts. *J. Mater. Chem. A* **2020**, *8*, 3541–3562. [[CrossRef](#)]

40. Pan, F.; Li, B.; Deng, W.; Du, Z.; Gang, Y.; Wang, G.; Li, Y. Promoting electrocatalytic CO₂ reduction on nitrogen-doped carbon with sulfur addition. *Appl. Catal. B* **2019**, *252*, 240–249. [[CrossRef](#)]
41. Zhao, J.; Chen, Z.; Zhao, J. Metal-free graphdiyne doped with sp-hybridized boron and nitrogen atoms at acetylenic sites for high-efficiency electroreduction of CO₂ to CH₄ and C₂H₄. *J. Mater. Chem. A* **2019**, *7*, 4026–4035. [[CrossRef](#)]
42. Li, G.; Pei, L.; Wu, Y.; Zhu, B.; Hu, Q.; Yang, H.; Zhang, Q.; Liu, J.; He, C. Facile synthesis of polyacrylonitrile-based N/S-codoped porous carbon as an efficient oxygen reduction electrocatalyst for zinc–air batteries. *J. Mater. Chem. A* **2019**, *7*, 11223–11233. [[CrossRef](#)]
43. Wang, G.; Liu, M.; Jia, J.; Xu, H.; Zhao, B.; Lai, K.; Tu, C.; Wen, Z. Nitrogen and Sulfur Co-doped Carbon Nanosheets for Electrochemical Reduction of CO₂. *ChemCatChem* **2020**, *12*, 2203–2208. [[CrossRef](#)]
44. Wang, H.; Shao, Y.; Mei, S.; Lu, Y.; Zhang, M.; Sun, J.-k.; Matyjaszewski, K.; Antonietti, M.; Yuan, J. Polymer-derived heteroatom-doped porous carbon materials. *Chem Rev.* **2020**, *120*, 9363–9419. [[CrossRef](#)] [[PubMed](#)]
45. Jin, H.; Feng, X.; Li, J.; Li, M.; Xia, Y.; Yuan, Y.; Yang, C.; Dai, B.; Lin, Z.; Wang, J. Heteroatom-doped porous carbon materials with unprecedented high volumetric capacitive performance. *Angew. Chem. Int. Ed.* **2019**, *131*, 2419–2423. [[CrossRef](#)]
46. Rangraz, Y.; Heravi, M.M.; Elhampour, A. Recent Advances on Heteroatom-Doped Porous Carbon/Metal Materials: Fascinating Heterogeneous Catalysts for Organic Transformations. *Chem Rec.* **2021**, *21*, 1985–2073. [[CrossRef](#)]
47. Rehman, A.; Nazir, G.; Rhee, K.Y.; Park, S.-J. A rational design of cellulose-based heteroatom-doped porous carbons: Promising condensers for CO₂ adsorption and separation. *Chem. Eng. J.* **2021**, *420*, 130421. [[CrossRef](#)]
48. Ashourirad, B.; Arab, P.; Islamoglu, T.; Cychosz, K.A.; Thommes, M.; El-Kaderi, H.M. A cost-effective synthesis of heteroatom-doped porous carbons as efficient CO₂ sorbents. *J. Mater. Chem. A* **2016**, *4*, 14693–14702. [[CrossRef](#)]
49. Li, M.; Wang, H.; Luo, W.; Sherrell, P.C.; Chen, J.; Yang, J. Heterogeneous single-atom catalysts for electrochemical CO₂ reduction reaction. *Adv. Mater.* **2020**, *32*, 2001848. [[CrossRef](#)]
50. Duan, X.; Xu, J.; Wei, Z.; Ma, J.; Guo, S.; Wang, S.; Liu, H.; Dou, S. Metal-free carbon materials for CO₂ electrochemical reduction. *Adv. Mater.* **2017**, *29*, 1701784. [[CrossRef](#)]
51. Zhang, X.; Xue, D.; Jiang, S.; Xia, H.; Yang, Y.; Yan, W.; Hu, J.; Zhang, J. Rational confinement engineering of MOF-derived carbon-based electrocatalysts toward CO₂ reduction and O₂ reduction reactions. *InfoMat* **2022**, *4*, e12257. [[CrossRef](#)]
52. Wang, T.; Zhao, Q.; Fu, Y.; Lei, C.; Yang, B.; Li, Z.; Lei, L.; Wu, G.; Hou, Y. Carbon-rich nonprecious metal single atom electrocatalysts for CO₂ reduction and hydrogen evolution. *Small Methods* **2019**, *3*, 1900210. [[CrossRef](#)]
53. Han, S.G.; Ma, D.D.; Zhu, Q.L. Atomically Structural Regulations of Carbon-Based Single-Atom Catalysts for Electrochemical CO₂ Reduction. *Small Methods* **2021**, *5*, 2100102. [[CrossRef](#)] [[PubMed](#)]
54. Wang, Y.; Shao, Y.; Wang, H.; Yuan, J. Advanced heteroatom-doped porous carbon membranes assisted by poly(ionic liquid) design and engineering. *Acc. Mater. Res.* **2020**, *1*, 16–29. [[CrossRef](#)] [[PubMed](#)]
55. Ahmed Ali, K.; Ahmad, M.I.; Yusup, Y. Issues, impacts, and mitigations of carbon dioxide emissions in the building sector. *Sustainability* **2020**, *12*, 7427. [[CrossRef](#)]
56. Jacobson, T.A.; Kler, J.S.; Hernke, M.T.; Braun, R.K.; Meyer, K.C.; Funk, W.E. Direct human health risks of increased atmospheric carbon dioxide. *Nature Sustain.* **2019**, *2*, 691–701. [[CrossRef](#)]
57. Gall, E.T.; Cheung, T.; Luhung, I.; Schiavon, S.; Nazaroff, W.W. Real-time monitoring of personal exposures to carbon dioxide. *Build. Environ.* **2016**, *104*, 59–67. [[CrossRef](#)]
58. Zheutlin, A.R.; Adar, S.D.; Park, S.K. Carbon dioxide emissions and change in prevalence of obesity and diabetes in the United States: An ecological study. *Environ. Int.* **2014**, *73*, 111–116. [[CrossRef](#)]
59. Zappulla, D. Environmental stress, erythrocyte dysfunctions, inflammation, and the metabolic syndrome: Adaptations to CO₂ increases? *CMSJ* **2008**, *3*, 30–34. [[CrossRef](#)]
60. Yang, X.-Y.; Chen, L.-H.; Li, Y.; Rooke, J.C.; Sanchez, C.; Su, B.-L. Hierarchically porous materials: Synthesis strategies and structure design. *Chem. Soc. Rev.* **2017**, *46*, 481–558. [[CrossRef](#)]
61. Sun, M.; Chen, C.; Chen, L.; Su, B. Hierarchically porous materials: Synthesis strategies and emerging applications. *Front. Chem. Sci. Eng.* **2016**, *10*, 301–347. [[CrossRef](#)]
62. Zhao, T.; Elzatahry, A.; Li, X.; Zhao, D. Single-micelle-directed synthesis of mesoporous materials. *Nat. Rev. Mater.* **2019**, *4*, 775–791. [[CrossRef](#)]
63. Liu, D.; Hu, Y.-Y.; Zeng, C.; Qu, D.-Y. Soft-templated ordered mesoporous carbon materials: Synthesis, structural modification and functionalization. *Acta Phys. Sin.* **2016**, *32*, 2826–2840. [[CrossRef](#)]
64. Xia, X.; Zhang, Y.; Fan, Z.; Chao, D.; Xiong, Q.; Tu, J.; Zhang, H.; Fan, H.J. Novel Metal@Carbon Spheres Core–Shell Arrays by Controlled Self-Assembly of Carbon Nanospheres: A Stable and Flexible Supercapacitor Electrode. *Adv. Energy Mater.* **2015**, *5*, 1401709. [[CrossRef](#)]
65. Liang, H.-W.; Wei, W.; Wu, Z.-S.; Feng, X.; Müllen, K. Mesoporous Metal–Nitrogen-Doped Carbon Electrocatalysts for Highly Efficient Oxygen Reduction Reaction. *J. Am. Chem. Soc.* **2013**, *135*, 16002–16005. [[CrossRef](#)] [[PubMed](#)]
66. Zhang, L.; Jiang, Y.; Wang, L.; Zhang, C.; Liu, S. Hierarchical porous carbon nanofibers as binder-free electrode for high-performance supercapacitor. *Electrochim. Acta* **2016**, *196*, 189–196. [[CrossRef](#)]
67. Wang, Q.; Yan, J.; Wang, Y.; Wei, T.; Zhang, M.; Jing, X.; Fan, Z. Three-dimensional flower-like and hierarchical porous carbon materials as high-rate performance electrodes for supercapacitors. *Carbon* **2014**, *67*, 119–127. [[CrossRef](#)]
68. He, X.; Zhang, N.; Shao, X.; Wu, M.; Yu, M.; Qiu, J. A layered-template-nanospace-confinement strategy for production of corrugated graphene nanosheets from petroleum pitch for supercapacitors. *Chem. Eng. J.* **2016**, *297*, 121–127. [[CrossRef](#)]

69. Fan, Z.; Liu, Y.; Yan, J.; Ning, G.; Wang, Q.; Wei, T.; Zhi, L.; Wei, F. Template-directed synthesis of pillared-porous carbon nanosheet architectures: High-performance electrode materials for supercapacitors. *Adv. Energy Mater.* **2012**, *2*, 419–424. [[CrossRef](#)]
70. Xie, K.; Qin, X.; Wang, X.; Wang, Y.; Tao, H.; Wu, Q.; Yang, L.; Hu, Z. Carbon nanocages as supercapacitor electrode materials. *Adv. Mater.* **2012**, *24*, 347–352. [[CrossRef](#)]
71. Cao, J.; Zhu, C.; Aoki, Y.; Habazaki, H. Starch-derived hierarchical porous carbon with controlled porosity for high performance supercapacitors. *ACS Sustain. Chem. Eng.* **2018**, *6*, 7292–7303. [[CrossRef](#)]
72. Qian, M.; Wang, Y.; Xu, F.; Zhao, W.; Lin, T.; Huang, F. Extraordinary porous few-layer carbons of high capacitance from pechini combustion of magnesium nitrate gel. *ACS Appl. Mater. Interfaces* **2018**, *10*, 381–388. [[CrossRef](#)] [[PubMed](#)]
73. Shao, J.; Song, M.; Wu, G.; Zhou, Y.; Wan, J.; Ren, X.; Ma, F. 3D carbon nanocage networks with multiscale pores for high-rate supercapacitors by flower-like template and in-situ coating. *Energy Storage Mater.* **2018**, *13*, 57–65. [[CrossRef](#)]
74. Wei, F.; Zhang, H.-f.; He, X.-j.; Ma, H.; Dong, S.-a.; Xie, X.-y. Synthesis of porous carbons from coal tar pitch for high-performance supercapacitors. *New Carbon Mater.* **2019**, *34*, 132–139. [[CrossRef](#)]
75. Jiang, L.; Wang, J.; Mao, X.; Xu, X.; Zhang, B.; Yang, J.; Wang, Y.; Zhu, J.; Hou, S. High rate performance carbon nano-cages with oxygen-containing functional groups as supercapacitor electrode materials. *Carbon* **2017**, *111*, 207–214. [[CrossRef](#)]
76. Wang, Q.; Yan, J.; Xiao, Y.; Wei, T.; Fan, Z.; Zhang, M.; Jing, X. Interconnected porous and nitrogen-doped carbon network for supercapacitors with high rate capability and energy density. *Electrochim. Acta* **2013**, *114*, 165–172. [[CrossRef](#)]
77. Wang, Q.; Yan, J.; Wei, T.; Feng, J.; Ren, Y.; Fan, Z.; Zhang, M.; Jing, X. Two-dimensional mesoporous carbon sheet-like framework material for high-rate supercapacitors. *Carbon* **2013**, *60*, 481–487. [[CrossRef](#)]
78. Zhao, Z.; Hao, S.; Hao, P.; Sang, Y.; Manivannan, A.; Wu, N.; Liu, H. Lignosulphonate-cellulose derived porous activated carbon for supercapacitor electrode. *J. Mater. Chem. A* **2015**, *3*, 15049–15056. [[CrossRef](#)]
79. Ma, X.; Gan, L.; Liu, M.; Tripathi, P.K.; Zhao, Y.; Xu, Z.; Zhu, D.; Chen, L. Mesoporous size controllable carbon microspheres and their electrochemical performances for supercapacitor electrodes. *J. Mater. Chem. A* **2014**, *2*, 8407–8415. [[CrossRef](#)]
80. Zeng, R.; Tang, X.; Huang, B.; Yuan, K.; Chen, Y. Nitrogen-Doped Hierarchically Porous Carbon Materials with Enhanced Performance for Supercapacitor. *ChemElectroChem* **2018**, *5*, 515–522. [[CrossRef](#)]
81. Li, J.; Jiang, Q.; Wei, L.; Zhong, L.; Wang, X. Simple and scalable synthesis of hierarchical porous carbon derived from cornstalk without pith for high capacitance and energy density. *J. Mater. Chem. A* **2020**, *8*, 1469–1479. [[CrossRef](#)]
82. Wei, F.; He, X.; Zhang, H.; Liu, Z.; Xiao, N.; Qiu, J. Crumpled carbon nanonets derived from anthracene oil for high energy density supercapacitor. *J. Power Sources* **2019**, *428*, 8–12. [[CrossRef](#)]
83. Wang, J.; Tang, J.; Ding, B.; Malgras, V.; Chang, Z.; Hao, X.; Wang, Y.; Dou, H.; Zhang, X.; Yamauchi, Y. Hierarchical porous carbons with layer-by-layer motif architectures from confined soft-template self-assembly in layered materials. *Nature Commun.* **2017**, *8*, 15717. [[CrossRef](#)]
84. Li, W.; Li, B.; Shen, M.; Gao, Q.; Hou, J. Use of Gemini surfactant as emulsion interface microreactor for the synthesis of nitrogen-doped hollow carbon spheres for high-performance supercapacitors. *Chem. Eng. J.* **2020**, *384*, 123309. [[CrossRef](#)]
85. Estevez, L.; Prabhakaran, V.; Garcia, A.L.; Shin, Y.; Tao, J.; Schwarz, A.M.; Darsell, J.; Bhattacharya, P.; Shutthanandan, V.; Zhang, J.-G. Hierarchically porous graphitic carbon with simultaneously high surface area and colossal pore volume engineered via ice templating. *ACS Nano* **2017**, *11*, 11047–11055. [[CrossRef](#)] [[PubMed](#)]
86. He, X.; Yu, H.; Fan, L.; Yu, M.; Zheng, M. Honeycomb-like porous carbons synthesized by a soft template strategy for supercapacitors. *Mater. Lett.* **2017**, *195*, 31–33. [[CrossRef](#)]
87. Peng, H.; Yao, B.; Wei, X.; Liu, T.; Kou, T.; Xiao, P.; Zhang, Y.; Li, Y. Pore and Heteroatom Engineered Carbon Foams for Supercapacitors. *Adv. Energy Mater.* **2019**, *9*, 1803665. [[CrossRef](#)]
88. Sun, L.; Zhou, H.; Li, L.; Yao, Y.; Qu, H.; Zhang, C.; Liu, S.; Zhou, Y. Double Soft-Template Synthesis of Nitrogen/Sulfur-Codoped Hierarchically Porous Carbon Materials Derived from Protic Ionic Liquid for Supercapacitor. *ACS Appl. Mater. Interfaces* **2017**, *9*, 26088–26095. [[CrossRef](#)]
89. Chen, L.-F.; Lu, Y.; Yu, L.; Lou, X.W. Designed formation of hollow particle-based nitrogen-doped carbon nanofibers for high-performance supercapacitors. *Energy Environ. Sci.* **2017**, *10*, 1777–1783. [[CrossRef](#)]
90. Fechler, N.; Fellingner, T.P.; Antonietti, M. “Salt templating”: A simple and sustainable pathway toward highly porous functional carbons from ionic liquids. *Adv. Mater.* **2013**, *25*, 75–79. [[CrossRef](#)]
91. Xie, X.; He, X.; Zhang, H.; Wei, F.; Xiao, N.; Qiu, J. Interconnected sheet-like porous carbons from coal tar by a confined soft-template strategy for supercapacitors. *Chem. Eng. J.* **2018**, *350*, 49–56. [[CrossRef](#)]
92. Fechler, N.; Zussblatt, N.P.; Rothe, R.; Schlögl, R.; Willinger, M.G.; Chmelka, B.F.; Antonietti, M. Eutectic syntheses of graphitic carbon with high pyrazinic nitrogen content. *Adv. Mater.* **2016**, *28*, 1287–1294. [[CrossRef](#)] [[PubMed](#)]
93. Xue, D.; Zhu, D.; Duan, H.; Wang, Z.; Lv, Y.; Xiong, W.; Li, L.; Liu, M.; Gan, L. Deep-eutectic-solvent synthesis of N/O self-doped hollow carbon nanorods for efficient energy storage. *Chem. Commun.* **2019**, *55*, 11219–11222. [[CrossRef](#)] [[PubMed](#)]
94. Li, Y.; Wang, G.; Wei, T.; Fan, Z.; Yan, P. Nitrogen and sulfur co-doped porous carbon nanosheets derived from willow catkin for supercapacitors. *Nano Energy* **2016**, *19*, 165–175. [[CrossRef](#)]
95. Ling, Z.; Wang, Z.; Zhang, M.; Yu, C.; Wang, G.; Dong, Y.; Liu, S.; Wang, Y.; Qiu, J. Sustainable Synthesis and Assembly of Biomass-Derived B/N Co-Doped Carbon Nanosheets with Ultrahigh Aspect Ratio for High-Performance Supercapacitors. *Adv. Funct. Mater.* **2016**, *26*, 111–119. [[CrossRef](#)]

96. Gao, F.; Qu, J.; Geng, C.; Shao, G.; Wu, M. Self-templating synthesis of nitrogen-decorated hierarchical porous carbon from shrimp shell for supercapacitors. *J. Mater. Chem. A* **2016**, *4*, 7445–7452. [[CrossRef](#)]
97. Ghosh, U.; Majumdar, A.; Pal, A. Photocatalytic CO₂ reduction over g-C₃N₄ based heterostructures: Recent progress and prospects. *J. Environ. Chem. Eng.* **2020**, *9*, 104631. [[CrossRef](#)]
98. Ong, W.-J.; Putri, L.K.; Mohamed, A.R. Rational Design of Carbon-Based 2D Nanostructures for Enhanced Photocatalytic CO₂ Reduction: A Dimensionality Perspective. *Eur. J. Chem.* **2020**, *26*, 9710–9748. [[CrossRef](#)]
99. Wei, D.; Liu, Y.; Wang, Y.; Zhang, H.; Huang, L.; Yu, G. Synthesis of N-doped graphene by chemical vapor deposition and its electrical properties. *Nano Lett.* **2009**, *9*, 1752–1758. [[CrossRef](#)]
100. Li, X.; Fan, L.; Li, Z.; Wang, K.; Zhong, M.; Wei, J.; Wu, D.; Zhu, H. Boron doping of graphene for graphene–silicon p–n junction solar cells. *Adv. Energy Mater.* **2012**, *2*, 425–429. [[CrossRef](#)]
101. Zhang, L.; Niu, J.; Li, M.; Xia, Z. Catalytic mechanisms of sulfur-doped graphene as efficient oxygen reduction reaction catalysts for fuel cells. *J. Phys. Chem. C* **2014**, *118*, 3545–3553. [[CrossRef](#)]
102. Wang, Y.; Zhang, C.; Li, X.; Gao, T.; Wang, X.-B. Metal-free carbon-based nanomaterials for electrochemical nitrogen and carbon dioxide reductions. *Mater. Res. Bull.* **2021**, *140*, 111294. [[CrossRef](#)]
103. Bing, X.; Wei, Y.; Wang, M.; Xu, S.; Long, D.; Wang, J.; Qiao, W.; Ling, L. Template-free synthesis of nitrogen-doped hierarchical porous carbons for CO₂ adsorption and supercapacitor electrodes. *J. Colloid Interface Sci.* **2017**, *488*, 207–217. [[CrossRef](#)]
104. Sun, Z.; Li, K.; Wee Koh, S.; Jiao, L. Low-Cost and Scalable Fabrication of Hierarchically Porous N-Doped Carbon for Energy Storage and Conversion Application. *ChemistrySelect* **2020**, *5*, 533–537. [[CrossRef](#)]
105. Liu, X.; Li, S.; Mi, R.; Mei, J.; Liu, L.-M.; Cao, L.; Lau, W.-M.; Liu, H. Porous structure design of carbon xerogels for advanced supercapacitor. *Appl. Energy* **2015**, *153*, 32–40. [[CrossRef](#)]
106. Li, H.; Xiao, N.; Hao, M.; Song, X.; Wang, Y.; Ji, Y.; Liu, C.; Li, C.; Guo, Z.; Zhang, F. Efficient CO₂ electroreduction over pyridinic-N active sites highly exposed on wrinkled porous carbon nanosheets. *Chem. Eng. J.* **2018**, *351*, 613–621. [[CrossRef](#)]
107. Zheng, Y.; Cheng, P.; Xu, J.; Han, J.; Wang, D.; Hao, C.; Alanagh, H.R.; Long, C.; Shi, X.; Tang, Z. MOF-derived nitrogen-doped nanoporous carbon for electroreduction of CO₂ to CO: The calcining temperature effect and the mechanism. *Nanoscale* **2019**, *11*, 4911–4917. [[CrossRef](#)] [[PubMed](#)]
108. Kuang, M.; Guan, A.; Gu, Z.; Han, P.; Qian, L.; Zheng, G. Enhanced N-doping in mesoporous carbon for efficient electrocatalytic CO₂ conversion. *Nano Res.* **2019**, *12*, 2324–2329. [[CrossRef](#)]
109. Li, F.; Xue, M.; Knowles, G.P.; Chen, L.; MacFarlane, D.R.; Zhang, J. Porous nitrogen-doped carbon derived from biomass for electrocatalytic reduction of CO₂ to CO. *Electrochim. Acta* **2017**, *245*, 561–568. [[CrossRef](#)]
110. Liu, S.; Yang, H.; Huang, X.; Liu, L.; Cai, W.; Gao, J.; Li, X.; Zhang, T.; Huang, Y.; Liu, B. Identifying active sites of nitrogen-doped carbon materials for the CO₂ reduction reaction. *Adv. Funct. Mater.* **2018**, *28*, 1800499. [[CrossRef](#)]
111. Li, W.; Herkt, B.; Sereych, M.; Bandoz, T.J. Pyridinic-N groups and ultramicropore nanoreactors enhance CO₂ electrochemical reduction on porous carbon catalysts. *Appl. Catal. B* **2017**, *207*, 195–206. [[CrossRef](#)]
112. Li, C.; Wang, Y.; Xiao, N.; Li, H.; Ji, Y.; Guo, Z.; Liu, C.; Qiu, J. Nitrogen-doped porous carbon from coal for high efficiency CO₂ electrocatalytic reduction. *Carbon* **2019**, *151*, 46–52. [[CrossRef](#)]
113. Ning, H.; Guo, D.; Wang, X.; Tan, Z.; Wang, W.; Yang, Z.; Li, L.; Zhao, Q.; Hao, J.; Wu, M. Efficient CO₂ electroreduction over N-doped hieratically porous carbon derived from petroleum pitch. *J. Energy Chem.* **2021**, *56*, 113–120. [[CrossRef](#)]
114. Wu, J.; Liu, M.; Sharma, P.P.; Yadav, R.M.; Ma, L.; Yang, Y.; Zou, X.; Zhou, X.-D.; Vajtai, R.; Yakobson, B.I. Incorporation of nitrogen defects for efficient reduction of CO₂ via two-electron pathway on three-dimensional graphene foam. *Nano Lett.* **2016**, *16*, 466–470. [[CrossRef](#)] [[PubMed](#)]
115. Zhu, X.; Tian, C.; Wu, H.; He, Y.; He, L.; Wang, H.; Zhuang, X.; Liu, H.; Xia, C.; Dai, S. Pyrolyzed triazine-based nanoporous frameworks enable electrochemical CO₂ reduction in water. *ACS Appl. Mater. Interfaces* **2018**, *10*, 43588–43594. [[CrossRef](#)]
116. Yao, P.; Qiu, Y.; Zhang, T.; Su, P.; Li, X.; Zhang, H. N-doped nanoporous carbon from biomass as a highly efficient electrocatalyst for the CO₂ reduction reaction. *ACS Sustain. Chem. Eng.* **2019**, *7*, 5249–5255. [[CrossRef](#)]
117. Shu, Z.; Ye, G.; Wang, J.; Liu, S.; He, Z.; Zhu, W.; Liu, B.; Liu, M. Nitrogen-doped carbon with high graphitic-N exposure for electroreduction of CO₂ to CO. *Ionics* **2021**, *27*, 3089–3098. [[CrossRef](#)]
118. Liu, W.; Qi, J.; Bai, P.; Zhang, W.; Xu, L. Utilizing spatial confinement effect of N atoms in micropores of coal-based metal-free material for efficiently electrochemical reduction of carbon dioxide. *Appl. Catal. B* **2020**, *272*, 118974. [[CrossRef](#)]
119. Ye, L.; Ying, Y.; Sun, D.; Zhang, Z.; Fei, L.; Wen, Z.; Qiao, J.; Huang, H. Highly Efficient Porous Carbon Electrocatalyst with Controllable N-Species Content for Selective CO₂ Reduction. *Angew. Chem. Int. Ed.* **2020**, *59*, 3244–3251. [[CrossRef](#)]
120. Song, Y.; Chen, W.; Zhao, C.; Li, S.; Wei, W.; Sun, Y. Metal-free nitrogen-doped mesoporous carbon for electroreduction of CO₂ to ethanol. *Angew. Chem.* **2017**, *129*, 10980–10984. [[CrossRef](#)]
121. Chen, K.; Deng, J.; Zhao, J.; Liu, X.; Imhanria, S.; Wang, W. Electrocatalytic Production of Tunable Syngas from CO₂ via a Metal-Free Porous Nitrogen-Doped Carbon. *Ind. Eng. Chem. Res.* **2021**, *60*, 7739–7745. [[CrossRef](#)]
122. Qin, Z.; Jiang, X.; Cao, Y.; Dong, S.; Wang, F.; Feng, L.; Chen, Y.; Guo, Y. Nitrogen-doped porous carbon derived from digested sludge for electrochemical reduction of carbon dioxide to formate. *Sci. Total Environ.* **2021**, *759*, 143575. [[CrossRef](#)] [[PubMed](#)]
123. Yuan, H.; Qian, X.; Luo, B.; Wang, L.; Deng, L.; Chen, Y. Carbon dioxide reduction to multicarbon hydrocarbons and oxygenates on plant moss-derived, metal-free, in situ nitrogen-doped biochar. *Sci. Total Environ.* **2020**, *739*, 140340. [[CrossRef](#)] [[PubMed](#)]

124. Li, W.; Fechler, N.; Bandosz, T.J. Chemically heterogeneous nitrogen sites of various reactivity in porous carbons provide high stability of CO₂ electroreduction catalysts. *Appl. Catal. B* **2018**, *234*, 1–9. [CrossRef]
125. Bandosz, T.J.; Ren, T.-Z. Porous carbon modified with sulfur in energy related applications. *Carbon* **2017**, *118*, 561–577. [CrossRef]
126. Wu, J.; Yadav, R.M.; Liu, M.; Sharma, P.P.; Tiwary, C.S.; Ma, L.; Zou, X.; Zhou, X.-D.; Jakobson, B.I.; Lou, J. Achieving highly efficient, selective, and stable CO₂ reduction on nitrogen-doped carbon nanotubes. *ACS Nano* **2015**, *9*, 5364–5371. [CrossRef]
127. Ni, W.; Xue, Y.; Zang, X.; Li, C.; Wang, H.; Yang, Z.; Yan, Y.-M. Fluorine doped cage-like carbon electrocatalyst: An insight into the structure-enhanced CO selectivity for CO₂ reduction at high overpotential. *ACS Nano* **2020**, *14*, 2014–2023. [CrossRef]
128. Xie, J.; Zhao, X.; Wu, M.; Li, Q.; Wang, Y.; Yao, J. Metal-free fluorine-doped carbon electrocatalyst for CO₂ reduction outcompeting hydrogen evolution. *Angew. Chem.* **2018**, *130*, 9788–9792. [CrossRef]
129. Sreekanth, N.; Nazrulla, M.A.; Vineesh, T.V.; Sailaja, K.; Phani, K.L. Metal-free boron-doped graphene for selective electroreduction of carbon dioxide to formic acid/formate. *Chem. Commun.* **2015**, *51*, 16061–16064. [CrossRef]
130. Li, W.; Seredych, M.; Rodríguez-Castellón, E.; Bandosz, T.J. Metal-free nanoporous carbon as a catalyst for electrochemical reduction of CO₂ to CO and CH₄. *ChemSusChem* **2016**, *9*, 606–616. [CrossRef]
131. Nakata, K.; Ozaki, T.; Terashima, C.; Fujishima, A.; Einaga, Y. High-yield electrochemical production of formaldehyde from CO₂ and seawater. *Angew. Chem. Int. Ed.* **2014**, *53*, 871–874. [CrossRef]
132. Li, W.; Bandosz, T.J. Analyzing the effect of nitrogen/sulfur groups' density ratio in porous carbons on the efficiency of CO₂ electrochemical reduction. *Appl. Surf. Sci.* **2021**, *569*, 151066. [CrossRef]
133. Yang, H.; Wu, Y.; Lin, Q.; Fan, L.; Chai, X.; Zhang, Q.; Liu, J.; He, C.; Lin, Z. Composition Tailoring via N and S Co-doping and structure tuning by constructing hierarchical pores: Metal-free catalysts for high-performance electrochemical reduction of CO₂. *Angew. Chem.* **2018**, *130*, 15702–15706. [CrossRef]
134. Li, R.; Liu, F.; Zhang, Y.; Guo, M.; Liu, D. Nitrogen, sulfur co-doped hierarchically porous carbon as a metal-free electrocatalyst for oxygen reduction and carbon dioxide reduction reaction. *ACS Appl. Mater. Interfaces* **2020**, *12*, 44578–44587. [CrossRef] [PubMed]
135. Cai, X.; Qin, B.; Li, Y.; Zhang, Q.; Yang, G.; Wang, H.; Cao, Y.; Yu, H.; Peng, F. Chlorine-Promoted Nitrogen and Sulfur Co-Doped Biocarbon Catalyst for Electrochemical Carbon Dioxide Reduction. *ChemElectroChem* **2020**, *7*, 320–327. [CrossRef]
136. Li, G.; Qin, Y.; Wu, Y.; Pei, L.; Hu, Q.; Yang, H.; Zhang, Q.; Liu, J.; He, C. Nitrogen and sulfur dual-doped high-surface-area hollow carbon nanospheres for efficient CO₂ reduction. *Chin. J. Catal.* **2020**, *41*, 830–838. [CrossRef]
137. Pan, F.; Liang, A.; Duan, Y.; Liu, Q.; Zhang, J.; Li, Y. Self-growth-templating synthesis of 3D N, P, Co-doped mesoporous carbon frameworks for efficient bifunctional oxygen and carbon dioxide electroreduction. *J. Mater. Chem. A* **2017**, *5*, 13104–13111. [CrossRef]
138. Xue, X.; Yang, H.; Yang, T.; Yuan, P.; Li, Q.; Mu, S.; Zheng, X.; Chi, L.; Zhu, J.; Li, Y. N, P-coordinated fullerene-like carbon nanostructures with dual active centers toward highly-efficient multi-functional electrocatalysis for CO₂RR, ORR and Zn-air battery. *J. Mater. Chem. A* **2019**, *7*, 15271–15277. [CrossRef]
139. Chen, S.; Liu, T.; Olanrele, S.O.; Lian, Z.; Si, C.; Chen, Z.; Li, B. Boosting electrocatalytic activity for CO₂ reduction on nitrogen-doped carbon catalysts by co-doping with phosphorus. *J. Energy Chem.* **2021**, *54*, 143–150. [CrossRef]
140. Liang, X.; Tian, N.; Zhou, Z.; Sun, S. N, P Dual-Doped Porous Carbon Nanosheets for High-Efficiency CO₂ Electroreduction. *ACS Sustain. Chem. Eng.* **2022**, *10*, 1880–1887. [CrossRef]
141. Liu, Y.; Zhang, Y.; Cheng, K.; Quan, X.; Fan, X.; Su, Y.; Chen, S.; Zhao, H.; Zhang, Y.; Yu, H. Selective electrochemical reduction of carbon dioxide to ethanol on a boron-and nitrogen-Co-doped nanodiamond. *Angew. Chem.* **2017**, *129*, 15813–15817. [CrossRef]
142. Ma, X.; Du, J.; Sun, H.; Ye, F.; Wang, X.; Xu, P.; Hu, C.; Zhang, L.; Liu, D. Boron, nitrogen co-doped carbon with abundant mesopores for efficient CO₂ electroreduction. *Appl. Catal. B* **2021**, *298*, 120543. [CrossRef]
143. Ghosh, S.; Ramaprabhu, S. Boron and nitrogen co-doped carbon nanosheets encapsulating nano iron as an efficient catalyst for electrochemical CO₂ reduction utilizing a proton exchange membrane CO₂ conversion cell. *J. Colloid Interface Sci.* **2020**, *559*, 169–177. [CrossRef]
144. Jia, C.; Ren, W.; Chen, X.; Yang, W.; Zhao, C. (N, B) Dual heteroatom-doped hierarchical porous carbon framework for efficient electroreduction of carbon dioxide. *ACS Sustain. Chem. Eng.* **2020**, *8*, 6003–6010. [CrossRef]
145. Yang, F.; Yu, H.; Mao, X.; Meng, Q.; Chen, S.; Deng, Q.; Zeng, Z.; Wang, J.; Deng, S. Boosting electrochemical CO₂ reduction on ternary heteroatoms-doped porous carbon. *Chem. Eng. J.* **2021**, *425*, 131661. [CrossRef]
146. Eid, K.; Ahmad, Y.H.; Mohamed, A.T.; Elsafy, A.G.; Al-Qaradawi, S.Y. Versatile synthesis of Pd and Cu Co-doped porous carbon nitride nanowires for catalytic CO oxidation reaction. *Catalysts* **2018**, *8*, 411. [CrossRef]
147. Eid, K.A.M.; Abdullah, A.M. *Carbon Nitride Nanostructures for Sustainable Energy Production and Environmental Remediation*; RSC: London, UK, 2021; Volume 51.
148. Eid, K.; Hailan, S.M.; Ibrahim, Y.S.; Salah, B.; Abdullah, A.M. Recent Advances in the Controlled Design of One-dimensional Carbon Nitrides for Thermal CO Oxidation Reaction. In *Carbon Nitride Nanostructures for Sustainable Energy Production and Environmental Remediation*; RSC: London, UK, 2021; pp. 1–37.
149. Ibrahim, Y.; Meslam, M.; Eid, K.; Salah, B.; Abdullah, A.M.; Ozoemena, K.I.; Elzatahry, A.; Sharaf, M.A.; Sillanpää, M. A review of MXenes as emergent materials for dye removal from wastewater. *Sep. Purif. Technol.* **2022**, *282*, 120083. [CrossRef]
150. Salah, B.; Eid, K.; Abdelgwad, A.M.; Ibrahim, Y.; Abdullah, A.M.; Hassan, M.K.; Ozoemena, K.I. Titanium Carbide (Ti₃C₂T_x) MXene Ornamented with Palladium Nanoparticles for Electrochemical CO Oxidation. *Electroanalysis* **2022**, *34*, 677–683. [CrossRef]

151. Ibrahim, Y.; Mohamed, A.; Abdelgawad, A.M.; Eid, K.; Abdullah, A.M.; Elzatahry, A. The recent advances in the mechanical properties of self-standing two-dimensional MXene-based nanostructures: Deep insights into the supercapacitor. *Nanomaterials* **2020**, *10*, 1916. [[CrossRef](#)]
152. Abdu, H.I.; Eid, K.; Abdullah, A.M.; Han, Z.; Ibrahim, M.H.; Shan, D.; Chen, J.; Elzatahry, A.A.; Lu, X. Unveiling one-pot scalable fabrication of reusable carboxylated heterogeneous carbon-based catalysts from eucalyptus plant with the assistance of dry ice for selective hydrolysis of eucalyptus biomass. *Renew. Energy* **2020**, *153*, 998–1004. [[CrossRef](#)]
153. Abdu, H.I.; Eid, K.; Abdullah, A.M.; Sliem, M.H.; Elzatahry, A.; Lu, X. Dry ice-mediated rational synthesis of edge-carboxylated crumpled graphene nanosheets for selective and prompt hydrolysis of cellulose and eucalyptus lignocellulose under ambient reaction conditions. *Green Chem.* **2020**, *22*, 5437–5446. [[CrossRef](#)]